

Supporting Information

The generalized solubility limit approach for vanadium based cathode materials for lithium-ion batteries

Arijit Mitra^a, Advait Gilankar^a, Saptarshi Das^b, Sambedan Jena^c, Debasish Das^c, Subhasish B. Majumder^b, Siddhartha Das^{a}*

^aDepartment of Metallurgical and Materials Engineering, Indian Institute of Technology Kharagpur, Kharagpur, West Bengal, India – 721302

^bMaterials Science Center, Indian Institute of Technology Kharagpur, Kharagpur, West Bengal, India – 721302

^cSchool of Nano Science and Technology, Indian Institute of Technology Kharagpur, Kharagpur, West Bengal, India - 721302

Corresponding Author

* Email: sdas@metal.iitkgp.ac.in; Phone : +91-3222-283256

Section S1: Experimental Section

Iron (III) nitrate nonahydrate (ACS Grade), polyvinyl alcohol, polymethyl methacrylate were procured from Merck. Dimethyl carbonate (>99%) was procured from Loba Chemie. Ammonium metavanadate (ACS Grade), LiPF_6 (Battery Grade), LiClO_4 (Battery Grade), 1,3-Dioxolane(Reagent Plus), 1,2-Dimethoxyethane (Reagent Plus), ethylene carbonate (98%) and commercial electrolyte were procured from Sigma Aldrich. Lithium Bis(Trifluoromethanesulfonyl) imide (>98%), fluoroethylene carbonate (FEC) (98%) were procured from Tokyo Chemicals Industry. Vanadium Pentoxide ($\geq 98\%$) was purchased from Sigma Aldrich, and used in its as-received condition. LiV_3O_8 was synthesized as per the recipe reported by Pan et al.¹ Commercial LiMn_2O_4 was purchased from Gelon LIB group, and used in its as-received form. All chemicals were used as received without further purification. All solutions for materials synthesis were made using deionized water.

S.1.1. Synthesis of Layered Fe-V-O Kazakhstanite:

In a 500 ml Borosil Reagent Bottle, 6 mmol of Ammonium Metavanadate was dissolved in 90 ml of water at 100°C on a digital hot plate cum stirring unit. In a separate beaker, 2 mmol of Iron (III) Nitrate was dissolved in 10 ml of water. The iron nitrate solution was added dropwise to the ammonium metavanadate solution under vigorous stirring to obtain yellow coloured suspension. The lid of the reagent bottle was closed and the hot plate temperature was raised to 120°C with stirring. The yellow suspension was kept under this condition for 4 hrs to obtain a brown coloured suspension. The sediments were filtered and washed several times using deionized water, and finally with acetone, to remove the contaminants. The desired powder was obtained after drying the solid products in a vacuum oven at 60°C .

S.1.2. Structural Characterization:

The as-prepared powders were structurally characterized using x-ray diffraction and electron microscopy techniques. X-ray diffractogram was obtained using a Bruker D8 Discover Diffractometer (equipped with sample alignment system using laser focusing) with $\text{Cu K}\alpha$ radiation ($\lambda=0.15418\text{nm}$). Another x-ray diffractogram was collected at the BL-12 Beamline, Indus-2 Synchrotron at a wavelength of 0.82463\AA for better resolution of the diffraction peaks. The Pawley Refinement of the obtained diffractogram was performed using GSAS-II Suite.² The Rietveld Refinement of the obtained diffractogram was performed using GSAS-II Suite. High resolution transmission electron micrographs, selected area diffraction patterns, x-ray elemental maps, along with bright and dark field STEM images were obtained using JEOL2100F TEM, operating at 200kV. Image processing of the micrographs was performed using ImageJ software.³ Scanning electron microscopy was performed using Zeiss Gemini 500 microscope, which includes the EDS spectroscopy of dissolution products on cycled separators from different

electrolytes using EDAX Elect Plus detector. Surface topography images along with surface potential maps of the particles were obtained in an atomic force microscope (Agilent 5500AFM), using a PPP-EFM Probe (Nanosensors). FTIR spectrum was collected from a range of 450 cm^{-1} to 4000 cm^{-1} using Nicolet 6700 (Thermo Fischer Scientific). Raman spectroscopy of the as-prepared powder was carried out using T64000 RAMAN spectrometer (Horiba) with Argon-Krypton mixed ion gas laser as excitation source having a wavelength of 532nm. Chemical oxidation states of the elements were identified using Thermo K-Alpha⁺ x-ray photoelectron spectroscopy (Thermo scientific). The best resolution of the x-ray photoelectron spectroscopy is 0.5eV FWHM at 1eV on Ag 3d peak, with an intensity of 4Mcps. The water content in the as-prepared powders was determined using TG/DTA Analysis performed in Netzsch STA449 under nitrogen atmosphere. The EDS analysis of the cycled separator in preliminary investigations was performed in FEI Inspect F50 scanning electron microscope (FEI), equipped with EDAX Octane Plus energy dispersive x-ray spectroscopy.

For ex-situ x-ray diffraction, the x-ray diffractogram was collected using a Bruker D8 Discover Diffractometer with Cu K _{α} radiation ($\lambda=0.15418\text{nm}$), in a 2-Theta Mode. The source angle was fixed at 5° for all the cases. The samples were aligned with the goniometer using the laser-based sample alignment apparatus present in the system. Ex-situ XPS was performed using synchrotron x-ray radiation having incident energy of 4.312 keV at INDUS-2 (Beamline-14) Facility. The XPS spectra were recorded using 15 keV Phoibos 225 HV hemispherical analyzer in a fixed analyzer transmission (FAT) mode. The survey scans & core-level scans were measured using step-size of 0.5 eV & 0.1 eV respectively with pass energy of 150 eV. Calibration of the scans was performed by taking the C1s binding energy to be 284.7eV. The peak fitting was performed using Fityk 0.9.8.⁴ Raman spectra of the cycled lithium counter electrodes were acquired using Witec Alpha 300R Raman Spectrophotometer (Witec, Germany) using an excitation wavelength of 532nm. The cycled lithium foils were sandwiched between a glass slide and glass cover slip, and sealed using DPX mountant inside the glove box prior to Raman measurements.

The phase purity of the as-received V₂O₅, as-prepared LiV₃O₈, and as-received LiMn₂O₄ was confirmed using x-ray diffraction experiments performed on a x-ray diffractometer (Bruker D8 Discover, Germany) in a Bragg-Brentano geometry with Cu-K _{α} radiation ($\lambda = 1.5406 \text{ \AA}$). The morphology of the as-received V₂O₅, as-prepared LiV₃O₈, and as-received LiMn₂O₄ was recorded using a field emission scanning electron microscope (Zeiss Gemini 500, Germany).

S.1.3. Electrochemical Characterization:

For Kazakhstanite phase, a viscous slurry was prepared by grinding the as-prepared powder (60 wt%), acetylene black (20 wt%), polyvinyl alcohol (15 wt%) and polymethyl methacrylate (5 wt%) in N-methyl-2-pyrrolidone in a vacuum mixer (MTI MSK-SFM-7). The slurry was then poured over battery grade Al current collector and tape cast using doctor blade. The coatings were first air dried in hot air oven at 60°C, followed by vacuum drying at 120°C. The same

coating procedure was adopted as well to obtain the coatings of LiV_3O_8 and LiMn_2O_4 . LiMn_2O_4 electrode coatings were prepared in a composition of active material: carbon black: binder = 7.5:1.5:1. LiV_3O_8 electrode coatings were prepared in a composition of active material: carbon black: binder = 3:1:1. The V_2O_5 electrode coatings were prepared over battery grade Al foil using an electrophoretic deposition technique reported by elsewhere.⁵⁻⁶ Circular electrode discs of 15 mm diameter were punched out using a disc cutter (MSK-T06 MTI Corporation, USA). Electrodes with different active material loading, ranging from 1.2 – 6mg (in 15mm discs), were tested. Lithium ion half-cell configuration of CR2032 coin cells were fabricated using the prepared electrodes, with lithium foil as counter and reference electrode. The electrolytes used in the tests were self-prepared inside an argon filled glove box with <0.5ppm for both H_2O and O_2 (MBraun Labstar Pro). The various compositions tested are listed in Table 1 (Manuscript), along with the separators used during testing. The coin cells were assembled in an argon filled glove box (Mbraun, Germany), with <0.5ppm levels for both O_2 and H_2O .

Galvanostatic charge discharge studies were carried out in automated battery testers (BST8-MA, MTI Corporation and BTS4000-5V10mA, Neware) between 1.5V-3.8V (for Kazakhstanite phase and V_2O_5), between 1.5V-4.0V (for LiV_3O_8), and between 3.0V-4.3V (for LiMn_2O_4) vs Li^+/Li redox couple. Gamry Series G750 Potentiostat-cum-Galvanostat was used for carrying out electrochemical impedance spectroscopy (EIS) measurements for cycled Kazakhstanite electrodes after 100 cycles (conducted at 3.8V in the frequency range of 100 kHz to 0.01Hz, with potentiostatic signal amplitude of 5 mV). EIS spectra were analyzed using ZSimpWin 3.21 program.⁷ Kramers-Kronig Extrapolation was performed on the impedance spectra for cycled electrochemical cell for a reliable fit of the experimental points with the proposed model.

The ionic conductivity of the electrolytes were measured using Autolab Microcell HC installed with TSC1600 closed electrochemical cell. The cell constant of the TSC1600 closed electrochemical cell was measured using 0.01D and 0.1D KCl solution at 25°C (as per NIST standards), and calculated to be 22.622 cm^{-1} . EIS spectra measured for the electrolytes, recorded between 100kHz and 100Hz, were analyzed using ZSimpWin 3.21 program and Nova 2.1.5.⁷

S.1.4. Molecular Dynamics Simulations Methodology

A stable version of Large-scale Atomic/Molecular Massively Parallel Simulator (LAMMPS – August 2019) was used for all the simulations.⁸⁻⁹ All the simulations were run on the Param-Shakti HPC Cluster, set up at IIT Kharagpur. Additional codes for cluster analysis were written in Python.

A three dimensional cubic simulation box consisting of Vanadium, Lithium, Hydroxide and Bistriflimide ions, along with 1-3 Dioxolane and 1-2 Dimethoxyethane molecules, was constructed using Packmol.¹⁰ The structures of Vanadium, Lithium, Hydroxide and Bistriflimide ions, along with 1-3 Dioxolane and 1-2 Dimethoxyethane molecules, were constructed using Avogadro.¹¹ Depending on the concentration of the salt added to solvent, the number of these

entities is varied in the initial simulation box, which is tabulated in Table 2 (Manuscript). All the initial configurations were relaxed using the energy minimization criteria, which adjusts the atom co-ordinates till a convergence criterion of 1E-05 was attained. The equilibration runs were first performed under NVE integration coupled with Langevin thermostat maintaining the temperature at 323K, to stabilize the phase space trajectory. This step was followed up by further runs in the NPT ensemble (323K temperature and 1 atm pressure) to allow for the simulation box to attain a stable volume and lowest possible energy configuration. Finally, the temperature was lowered to 300K in the NPT ensemble at 1atm pressure to generate equilibrated systems for further production runs. The total time for equilibration was over 20 ns to ensure that proper mixing has taken place, and any stray effects from the initially assembled systems are eliminated.

The bonded and non-bonded force-field parameters for DOL and DME were taken from OPLS-AA, which is also available within the Moltemplate package.¹²⁻¹³ The non-bonded interactions consist of pairwise Lennard-Jones and coulombic interactions, with a cutoff distance of 10Å. The long range electrostatic interactions were computed using the PPPM method, with an accuracy of 0.0001. The LJ pairwise interaction parameters of unlike atoms were calculated from the Lorentz-Berthelot mixing rules. The bonded and non-bonded force-field parameters for TFSI anion was taken from the results reported by Lopes et al.¹⁴ The bonded and non-bonded force-field parameters for hydroxide ion were taken from the TIP3P water model.¹⁵ The force-field parameters for lithium and vanadium ions were taken from results reported by Pluhařová et al. and Gupta et al., respectively.¹⁶⁻¹⁷ The partial charges for DOL, DME, and TFSI were obtained from Atomic Charge Calculator II, maintained by Masaryk University.¹⁸ The partial charges were scaled down by a factor of 0.67 ($\sim \sqrt{1/\eta_\infty}$), to reflect the charge screening effect absent in non-polarizable force-fields.¹⁹⁻²⁰

The density of the electrolytes was calculated by taking the average density obtained post equilibration runs. The self-diffusion coefficients of the ions were calculated from the Einstein form of the Green-Kubo relations, where the intercept of the Mean Square Displacement (MSD) vs time in log-log scale is equal to the self-diffusion coefficient. The ionic conductivity of the electrolytes was calculated from the Einstein form of the ionic conductivity, while accounting for ionic interactions, as described by France-Lanord et al.²¹ The production runs for calculation of MSD and ionic conductivity was of duration of 20 ns and 5 ns, respectively. The shear viscosity of the electrolytes was calculated from the Reversible Equilibrium Molecular Dynamics (REMD) scheme described by Muller-Planthe.²² The de-solvation energy of the vanadium ions in the electrolytes was calculated from the Free-Energy Perturbation (FEP) and Finite Difference Thermodynamic Integration (FDTI) technique, wherein the non-bonded LJ parameters and the partial charges of V-OH assembly was varied while measuring the total energy change in the system.²³⁻²⁴ The partial charges and the LJ parameters were ramped down from a scale factor of 1 to 0 in a step of 0.05, while equilibrating the system for 500 ps before the next scaling was performed. Ion dynamics was studied by implementing self-designed algorithms on the output generated after MD runs.

Section S2: FMEA Analysis

Table S3: FMEA table to identify the major cause of degradation of cathode materials

Process: Cycleability of cathode materials					
Failure Modes	Severity (A)	Probability of Occurance (B)	Probability of Detection (C)	Risk Preference Number (RPN)	Reasoning
	Rank - 1 to 10	Rank - 1 to 10	Rank - 1 to 10	(A) * (B) * (C).	
	10 - Most Severe	10 - Highest Probability	10 - Highly undetectable		
Irreversible Phase Transformations in 1st cycle	4	10	2	80	Charge-discharge profile of the 1st cycle is different from rest of the cycles
Continuous Irreversible Phase Transformations post 1st cycle	7	9	9	567	Occurs in almost all the known cathode materials, difficult to quantify without dismantling the cell.
CEI degradation	7	6	6	252	Occurs only in high voltage cathode materials, quantifiable by impedance spectroscopy and DCIR techniques
Electrode Delamination	10	2	2	40	Discontinuous drop in cycleability followed by rapid decay of capacity. Can be detected from

					cycleability plot.
Active Material Dissolution	10	6	9	540	Usually gets convoluted with continuous irreversible phase transformation and capacity decay is mistakenly clubbed with it. Cannot be detected without dismantling the cell and performing spectroscopic analysis on the components. Known to occur in V and Mn based cathode materials and other high voltage cathodes.
Poor Current Collector Passivation	9	2	9	162	Only occurs at very high voltages due to improper passivation by the decomposed products over the current collector

Section S3: Structural and additional electrochemical characterization for Kazakhstanite Phase

S.3.1. Structural aspects of the Kazakhstanite phase (Compiled)

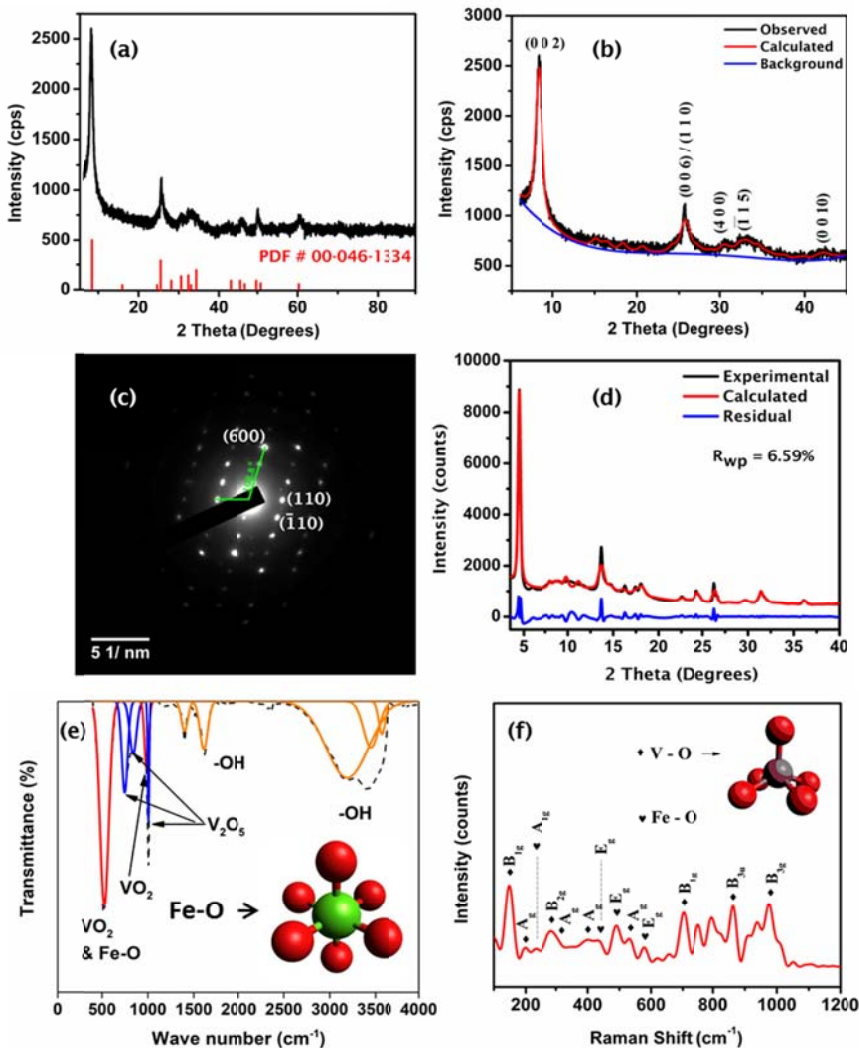


Figure S1. (a) X-ray diffractogram of the as-prepared powders, whose peaks are matched with the ICDD PDF Card for Kazakhstanite phase (00-046-1334). (b) Pawley refinement of the x-ray diffractogram for confirmation of phase matching and indexing. (c) Selected area diffraction pattern for as-prepared powder along ZA (001). (d) Rietveld refined x-ray diffractogram with the proposed unit cell model of Kazakhstanite phase. (e) Fourier-Transform Infrared spectrum of as-prepared powder, with the co-ordination geometry of Fe-O bonds represented inset. (f) Raman spectrum of as-prepared powder, with the co-ordination geometry of V-O bonds represented inset.

Figure S1(a) shows the X-ray diffractogram of the as-prepared Kazakhstanite powders. The peaks obtained from the diffractograms match with the Kazakhstanite type phase (PDF # 00-046-1334). The data card does not contain the atomic positions of the elements present in the Kazakhstanite structure. However, the chemical formula is presented as $\text{Fe}_5^{3+}\text{V}_3^{4+}\text{V}_{12}^{5+}\text{O}_{39}(\text{OH})_9 \cdot 9\text{H}_2\text{O}$, along with the lattice details (space group and lattice parameters). The iron atoms are expected to be in their +3 state, with the vanadium atoms present in both +4 and +5 states. With the lattice details provided in the data card as a starting point for further structural elucidation, a Pawley refinement of the collected spectrum is performed (Figure S1(b)), which provides a good match with the unit cell parameters presented in the data card. The space-group of the phase is identified to be C2/m with the unit cell parameters as $a = 11.84 \text{ \AA}$, $b = 3.66 \text{ \AA}$, $c = 21.58 \text{ \AA}$ and $\beta = 98.55^\circ$. The unit-cell parameters are confirmed by indexing an electron diffraction pattern which is obtained for the as-prepared powder, as shown in Figure S1(c). Figures S1(e)-(f) show the Fourier Transform Infrared and Raman spectra of the as-prepared material, from $100\text{cm}^{-1} - 1200\text{cm}^{-1}$ (Raman) and $400\text{cm}^{-1} - 4000\text{cm}^{-1}$ (FTIR). Peak deconvolution in the Raman spectra reveals the stretching and bending vibrations of V-O and Fe-O co-ordinations present within the material. The positions for the V-O vibrations are very similar to the ones observed for V_2O_5 .²⁵ Since, the structure is a layered one based on vanadium oxide, we believe that the structure should be very close to that of V_2O_5 . It is also observed that the lattice parameters of the Kazakhstanite phase are nearly integral multiples of the lattice parameters of V_2O_5 . Thus, the Kazakhstanite phase is expected to be constructed in similar fashion as V_2O_5 , wherein the unit cell consists of alternating V-O square-pyramidal polyhedral arranged in a layered fashion. The vibrations, indexed to Fe-O bonds in FTIR and Raman Spectra, indicate that they are present in an octahedral co-ordination. Additionally, the presence of O-H bond is also indicated in the FTIR Spectrum. The reported chemical formula in the literature indicates that the phase contains about 9 molecules of water.²⁶ This is confirmed by performing a thermogravimetric analysis, the results of which is reported in this file below (Figure S4: Section S.3.2.). Thus, the Kazakhstanite phase consists of V-O square pyramidal and Fe-O octahedral units arranged in a layered fashion, with few of the O replaced by OH and H_2O . Based on the above findings, a set of atomic positions are created for the V, Fe and O atoms such that above conclusions are satisfied. This set of atomic co-ordinates for Fe, V and O are added to the data card and used for Rietveld Refinement with the experimental diffractogram obtained at the BL-12 Beamline of Indus-2 synchrotron facility. This diffractogram is used for this analysis since the one obtained with the lab Cu- K_α is not of sufficient quality for this purpose. As shown in Figure S1(d), the calculated x-ray spectrum matches well with the experimental x-ray spectrum, with R_{wp} of 6.59%. Thus, the atomic co-ordinates deduced from spectroscopic and diffraction experiments can be accepted for future studies in this manuscript. The proposed unit cell for Kazakhstanite phase is presented in Supporting Information (Section S.3.3.).

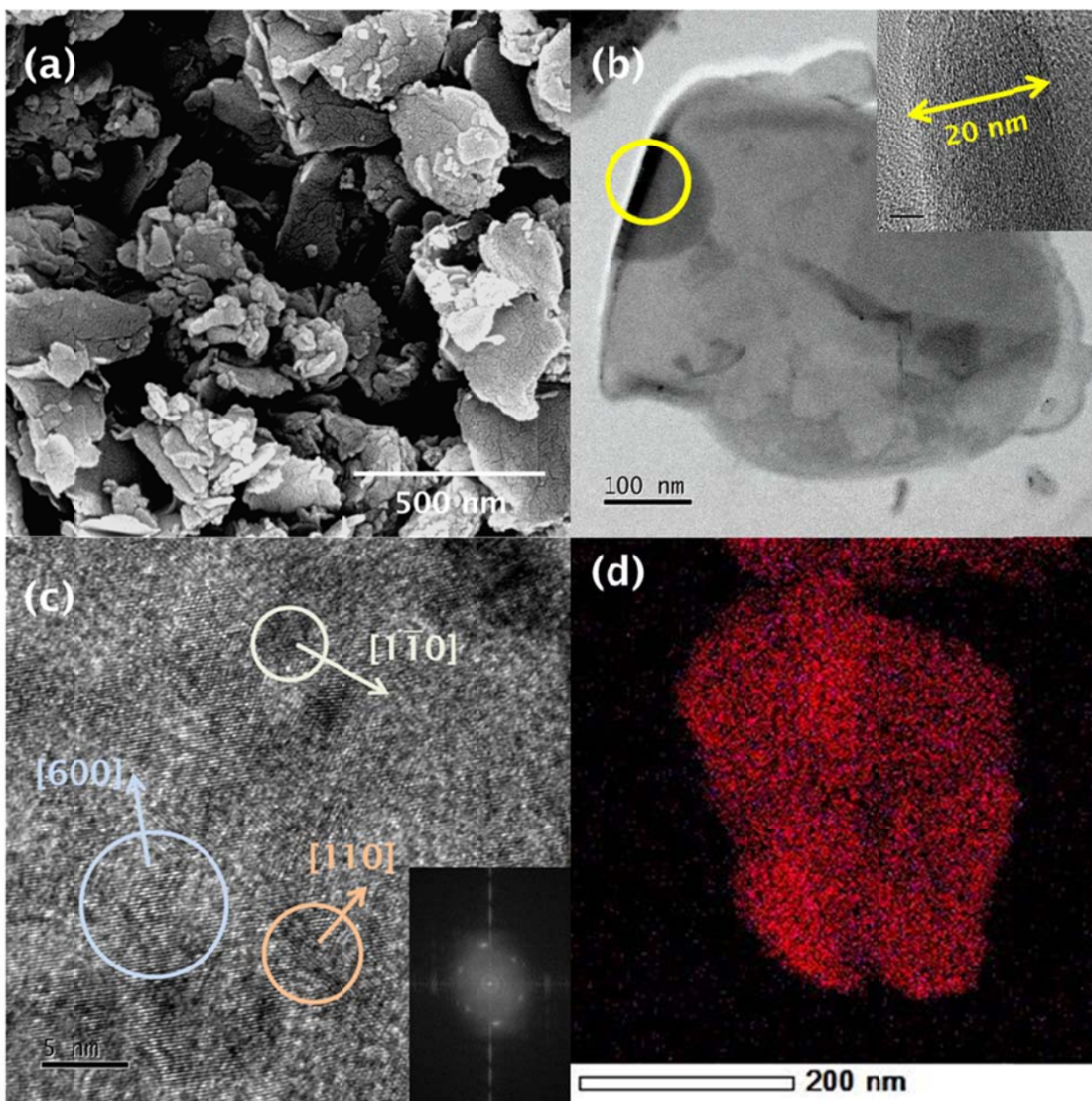


Figure S2: (a) Scanning electron micrograph of as-prepared Kazakhstanite powder, indicating the flake type morphology of the particles. (b) Transmission electron micrograph of one isolated particle, indicating the width of the flake to be about 20nm (inset). (c) HRTEM image in the bulk region of the particle shown in (b), indicating the various lattice fringes and their directions along with the FFT spectrum in inset. (d) EDS overlay map of Fe and V, indicating a uniform distribution of the two elements in the as-prepared Kazakhstanite powder.

Figure S2 shows the scanning and transmission electron micrographs of the as-prepared powders. The morphology of the particles in the as-prepared powders, as shown in Figure S2(a), is flake-type. The unit cell calculated from the diffraction experiments indicate that the two of

the dimensions of the unit cell are quite large (a and c). If the size of flakes (along these axes) is not large with respect to the unit cell dimensions, then peak broadening will be observed in the diffractograms. This is very well confirmed from the scanning electron micrographs. The flake-type morphology has one of its dimensions within 100 nm, which is responsible for peak broadening in the x-ray spectrum. It is due to this particular morphology that the ab-initio structure determination from x-ray diffraction is difficult. The transmission electron micrographs (Figure S2(b)) show that the thickness of the flake is within 20nm (circled region). The fringe spacing along this thickness is measured to be ~ 0.37 nm, which is close to the d-spacing of (0 0 6) plane. The flake appears to be bent in the circled region in Figure S2(b), which can be used in identifying the thickness. This indicates that the bulk of the flake, outside the circled region in Figure S2(b), should be oriented along [0 0 1] zone axis. This is confirmed by indexing the selected area diffraction pattern shown in Figure S1(c). The selected area diffraction pattern shown in Figure S1(c) is collected from the region of interest shown in Figure S2(b). As indicated in Figure S2(c), a high resolution image in the bulk of the flake shows lattice fringes, which is identified post indexing the FFT spectrum of image. The EDS map of the particle reveals both iron and vanadium to be present uniformly, at an atomic fraction of 1:3 (Figure S2(d)). The individual maps of Fe and V used for overlay are provided in this file below (Figure S8: Section S.3.5).

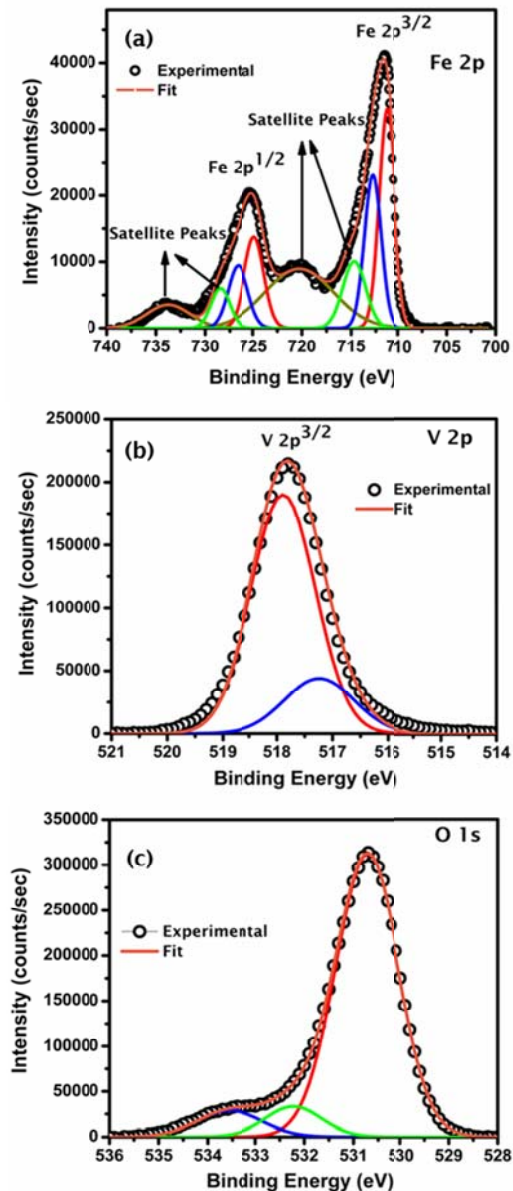


Figure S3: Core level XPS spectra for (a) Fe 2p, (b) V 2p, and (c) O 1s, indicating the various oxidation states of the elements present in the as-prepared Kazakhstanite powders along with their peak de-convolution.

Figure S3 shows the core level X-ray photoelectron spectrum of the as-prepared powders, for O, V and Fe. The position of the peaks in Fe 2p^{3/2} core level spectrum indicates that it is present in its +3 oxidation state. There are two peaks for Fe³⁺ state observed post deconvolution. This may indicate that Fe is not co-ordinated by similar anions. The water molecule and hydroxide anion must be co-ordinated to iron atoms in the Kazakhstanite phase. From the V2p^{3/2} core level spectrum, it is observed that the vanadium is present in its +4 and +5 state. The ratio of the oxidation states, determined from the area, is close to 1:4, which matches well with the chemical

formula reported in the literature. A deconvolution of O1s core level spectrum reveals the presence of three peaks. This is due to the presence of oxygen in three forms, i.e., oxide, hydroxide, and structural water molecule, in the Kazakhstanite phase. From the intensity calculations, it is observed that the Fe and V atoms are present in a ~1:3 atomic concentration ratio, which matches well with the reported chemical formula in the literature and the EDS results (Supporting Information File Section S.3.6.).

S.3.2. Thermogravimetric Analysis

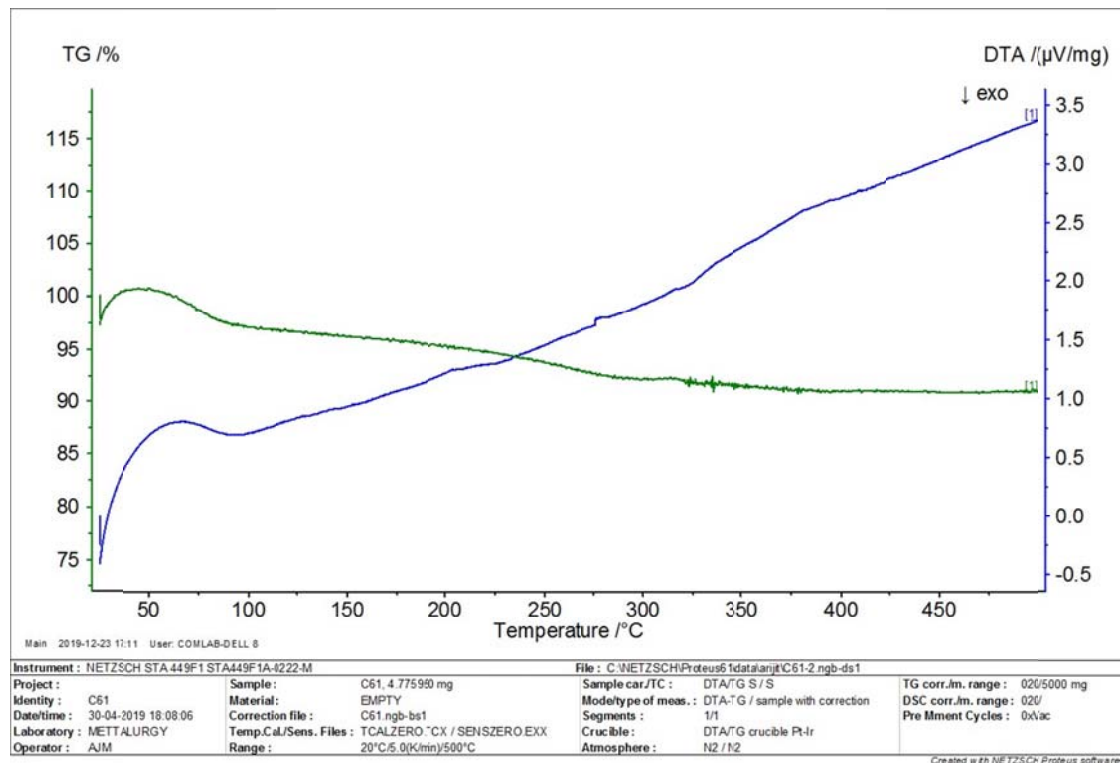


Figure S4: TG curve for the as-prepared powder, indicating the mass changes against temperature, along with DTA signals recorded.

The thermogravimetric curves indicate that there is a total of ~9% loss in mass when the sample is heated to 500°C. The DTA signals indicate that there should be no phase transformation occurring in this temperature range. Therefore, the mass loss can be attributed to loss of structural water. The calculations indicate that about 9 molecules of water are present in the material.

S.3.3. Unit-Cell Determination

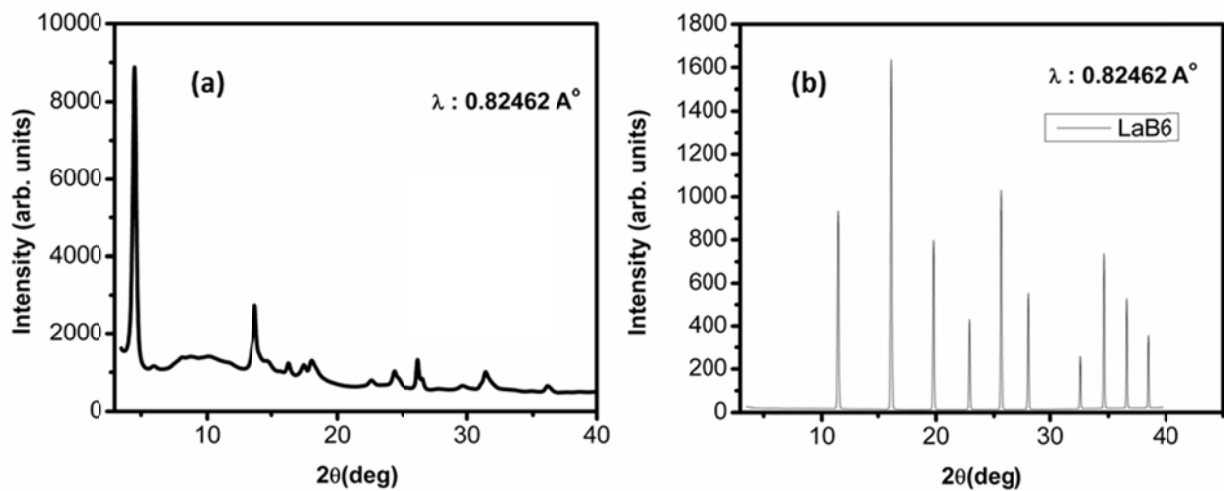


Figure S5: (a) Synchrotron X-ray Diffraction pattern obtained from BL-14 Beamline at Indus 2 for as-prepared powder. (b) Synchrotron X-ray Diffraction pattern for standard LaB₆ to obtain diffractometer parameters.

Figure S5(a) shows the synchrotron X-ray Diffraction results for the as-prepared Kazakhstanite phase. The broad peaks along with few indistinct features do not allow for an ab-initio structure determination experiment. From the microstructural analysis, it is observed that peak broadening occurs due to small thickness of the particles/crystallites (~20nm). Figure S5(b) shows the Synchrotron X-ray Diffraction pattern for standard LaB₆ to obtain diffractometer parameters.

The details of the proposed unit cell are provided below, with the unit cell representation along ac and ab planes shown in Figure S6.

```
_pd_phase_name Kaz
_cell_length_a 11.861(7)
_cell_length_b 3.6613(18)
_cell_length_c 21.076(18)
_cell_angle_alpha 90
_cell_angle_beta 98.98(6)
_cell_angle_gamma 90
_cell_volume 904.1(4)
_exptl_crystal_density_diffn 3.179
_symmetry_cell_setting monoclinic
_symmetry_space_group_name_H-M "C 2/m"
loop_
  _space_group_symop_id
  _space_group_symop_operation_xyz
```

- 1 x,y,z
- 2 -x,y,-z
- 3 -x,-y,-z
- 4 x,-y,z
- 5 1/2+x,1/2+y,z
- 6 1/2-x,1/2+y,-z
- 7 1/2-x,1/2-y,-z
- 8 1/2+x,1/2-y,z

ATOMIC COORDINATES AND DISPLACEMENT PARAMETERS

loop_

	_atom_site_label	_atom_site_type_symbol	_atom_site_fract_x	_atom_site_fract_y	_atom_site_fract_z	_atom_site_occupancy	_atom_site_adp_type	_atom_site_U_iso_or_equiv	_atom_site_symmetry_multiplicity
V1	V		0.37500	0.00000	0.09660	0.500	Uiso	0.010	4
V2	V		0.37500	0.50000	0.92966	0.500	Uiso	0.010	4
V3	V		0.37500	0.50000	0.59633	0.500	Uiso	0.010	4
V4	V		0.37500	0.00000	0.43000	0.500	Uiso	0.010	4
V5	V		0.37500	0.00000	0.76332	1.000	Uiso	0.010	4
O6	O		0.37500	0.00000	0.18000	1.000	Uiso	0.010	4
O7	O		0.37500	0.00000	0.32544	1.000	Uiso	0.010	4
O8	O		0.37500	0.00000	0.51333	0.500	Uiso	0.010	4
O9	O		0.37500	0.50000	0.67874	1.000	Uiso	0.010	4
O10	O		0.37500	0.00000	0.84665	1.000	Uiso	0.010	4
O11	O		0.37500	0.50000	0.01200	0.500	Uiso	0.010	4
O12	O		0.25000	0.25000	0.08330	0.500	Uiso	0.010	8
O13	O		0.50000	0.25000	0.08330	1.000	Uiso	0.010	8
O14	O		0.25000	0.25000	0.25000	0.500	Uiso	0.010	8
O15	O		0.50000	0.25000	0.25000	1.000	Uiso	0.010	8
O16	O		0.25000	0.25000	0.41668	0.500	Uiso	0.010	8
O17	O		0.50000	0.25000	0.41668	1.000	Uiso	0.010	8
O18	O		0.25000	0.25000	0.91665	1.000	Uiso	0.010	8
O19	O		0.50000	0.25000	0.91665	1.000	Uiso	0.010	8
Fe20	Fe		0.37500	0.00000	0.25000	1.000	Uiso	0.010	4

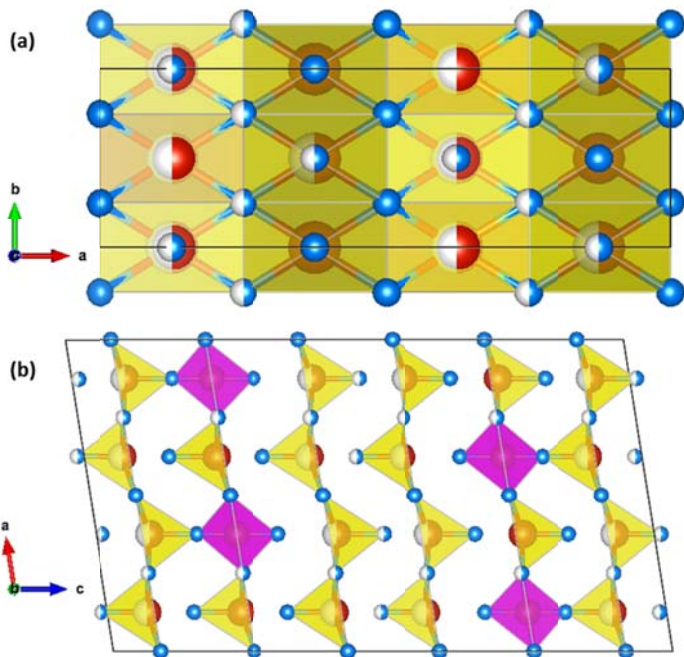


Figure S6: Proposed Unit cell representation of the kazakhstanite phase, created using VESTA. The unit cell is represented along ab **(a)** and ac **(b)** planes.

S.3.4. Calculations on electron diffraction patterns

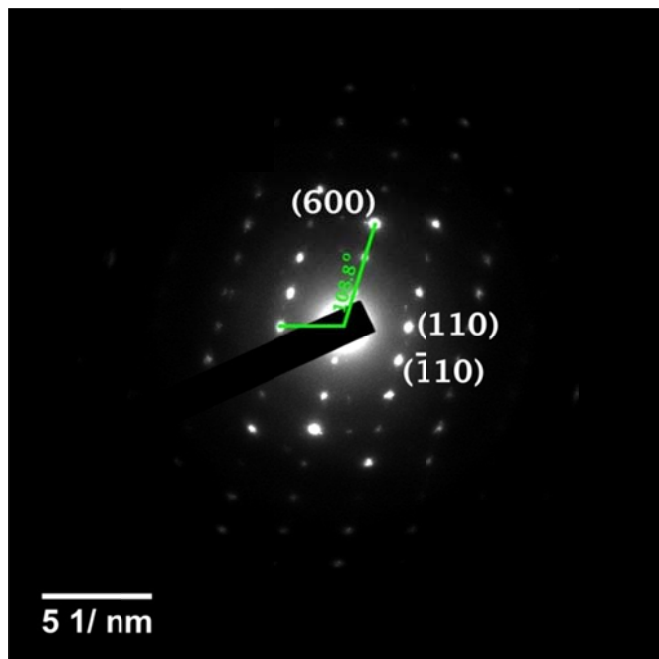


Figure S7: Selected Area Diffraction Pattern collected from a thin, isolated particle of the as-prepared material. The spots are indexed in the above pattern, along with the angles calculated using Image J.

Post pawley refinement of the X-ray diffractogram of the as-prepared powder for phase identification, a possible solution obtained was for a space group C2/m with lattice parameters $a = 11.84\text{\AA}$, $b = 3.66\text{\AA}$, $c = 21.58\text{\AA}$ and $\beta = 98.55^\circ$. The angle between two sets of planes $(h_1k_1l_1)$ and $(h_2k_2l_2)$ can be calculated as:

$$\begin{aligned} \phi = \cos^{-1} & \left\{ 1.022 * \left[\sqrt{0.00713h_1^2 + 0.0731l_1^2 + 0.00214k_1^2 + 2.908e^{-4}h_1l_1} \right]^{-1} \right. \\ & * \left. \left[\sqrt{0.00713h_2^2 + 0.0731l_2^2 + 0.00214k_2^2 + 2.908e^{-4}h_2l_2} \right]^{-1} \right. \\ & * \left. \begin{bmatrix} 0.0073 & 0 & 5.95e^{-4} \\ h_1 & k_1 & l_1 \\ 0 & 0.075 & 0 \\ 5.95e^{-4} & 0 & 0.0022 \end{bmatrix} \begin{bmatrix} h_2 \\ k_2 \\ l_2 \end{bmatrix} \right\} \end{aligned}$$

Therefore, by putting appropriate (hkl) values, angle between two planes can be calculated. Angle between (110) and (600) is calculated as 71.8° , which is close to the experimental value. The distance of the spots from the transmitted beam, for each of the indexed spots, match well with the calculated values.

S.3.5. STEM-EDS Maps

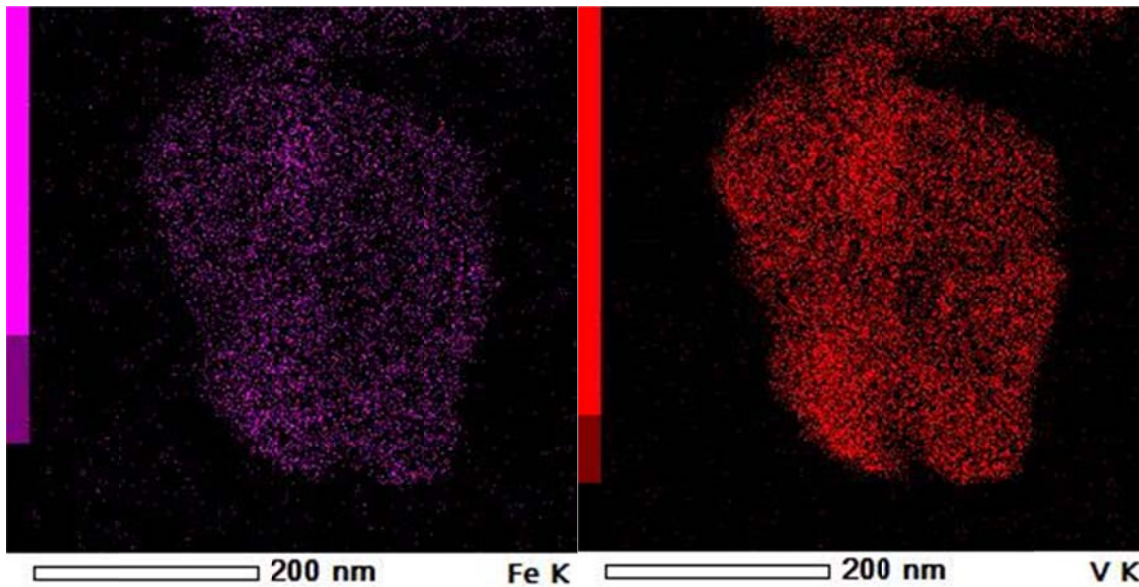
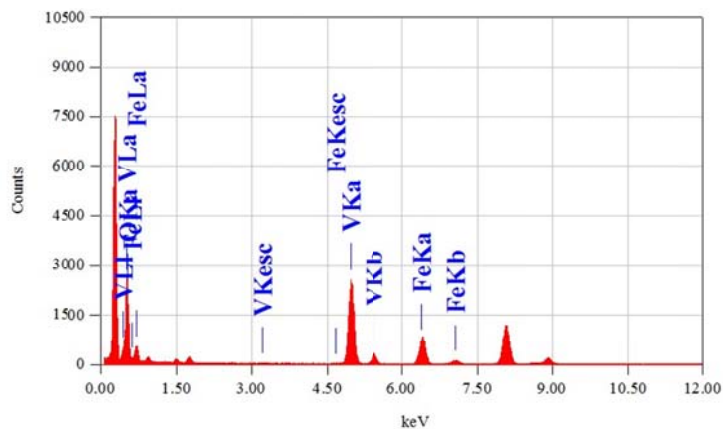


Figure S8: STEM-EDS maps of the Fe and V elements which are used for overlay map shown in Figure S2(d).



Acquisition Parameter
 Instrument : JEM-2100F
 Acc. Voltage : 200.0 kV
 Probe Current: 1.00000 nA
 PHA mode : T3
 Real Time : 131.07 sec
 Live Time : 128.88 sec
 Dead Time : 1 %
 Counting Rate: 1425 cps
 Energy Range : 0 - 40 keV

Thin Film Standardless Standardless Quantitative Analysis

Fitting Coefficient : 0.5272

Element	(keV)	Mass%	Counts	Sigma	Atom%	Compound	Mass%	Cation
O K	0.525	18.42	7345.83	0.34	42.40			1.3
V K (Ref.)	4.949	59.95	31122.76	0.67	43.34			1.0
Fe K	6.398	21.63	9881.98	0.43	14.27			1.1
Total		100.00			100.00			

Figure S9: EDS Results from Scanning Transmission Electron Microscopy Experiment for as-prepared powders.

S.3.6. XPS Composition Determination

Table S4 shows the tabulated results from XPS analysis for composition determination of as-prepared powder. Since H cannot be identified and analysed using XPS, the ratio of Fe to V is used in order to identify whether the stoichiometry reported in the literature is valid or not. It is observed that Fe:V atomic ratio is close to 1:3, which corresponds well with the literature reported value.

Table S4: XPS Elemental Analysis for Composition Estimation.

Element	Area	RSF	Area/RSF	Conc
Fe	119768	2.957	40503.213	3.95431
V	277044	2.116	130928.17	12.78246
O	606375.5	0.711	852848.8	83.26323
			1024280.2	

S.3.7. Ex-Situ XRD and XPS Plots:

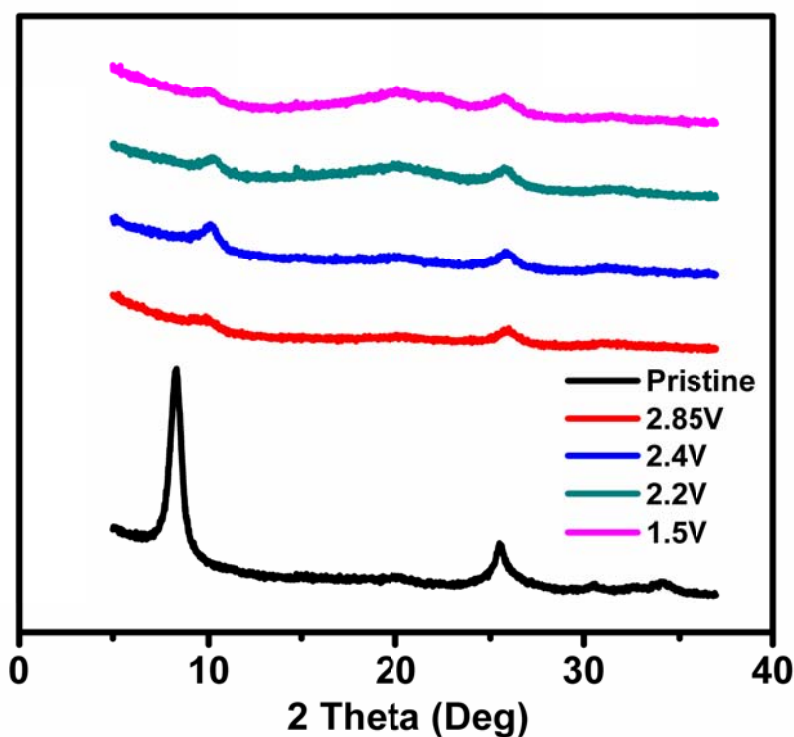


Figure S10: Ex-situ X-ray Diffractograms of the electrode coatings at different states of charge.

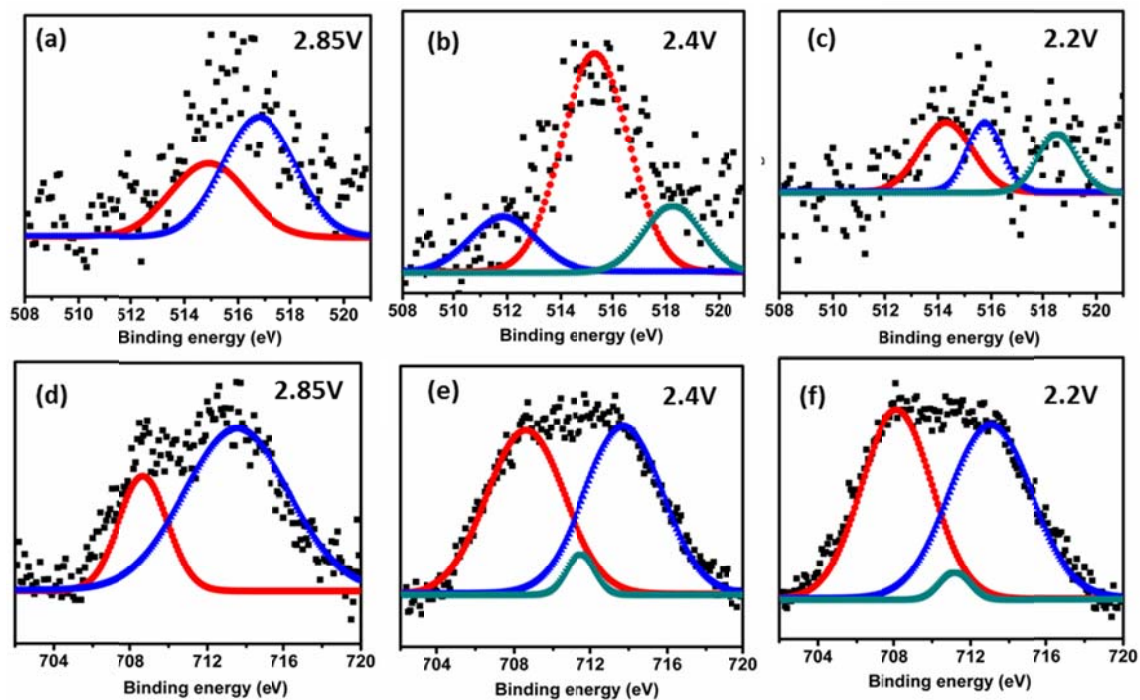


Figure S11: (a)-(c) $V2p^{3/2}$ and (d)-(f) $Fe2p$ fits for electrode coatings at different states of charge

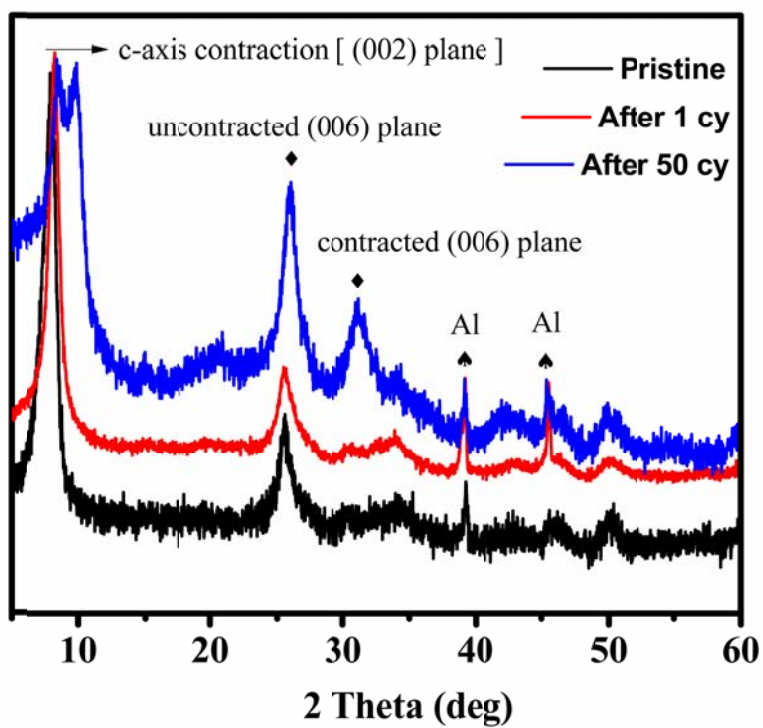


Figure S12: X-ray diffractograms of the cycled electrodes

From Bragg's Law:

$$2d\sin\theta = n\lambda = \text{constant (Cu } K_{\alpha} \text{ radiation)}$$

$$\text{Therefore, } d_{002}\sin\theta_{002} = \frac{1}{3} d_{002}\sin\theta_{006}$$

For uncontracted c-axis, $\sin\theta_{002} \cong 0.149$. Therefore, $\theta_{006} \cong 25.98^{\circ}$

For contracted c-axis, $\sin\theta_{002} \cong 0.171$. Therefore, $\theta_{006} \cong 30.87^{\circ}$

S.3.8. Supporting electrochemical results from the battery cyclers:

We have deduced two possible reasons for this based on the ex-situ XRD and XPS results. The first possible reason can be electrolyte degradation due to release of structural water, which affects the charge-transfer reaction at the electrode-electrolyte interface. The second possible reason is that the ionic compound formed at the end of the plateau region is soluble in the electrolyte, thereby creating a situation of the loss of active material. In order to determine whether the first case is the cause for the poor cycleability, another cycleability test is conducted with the LCL electrolyte, wherein the LiClO_4 salt will not be degraded by the release of water molecules. To our surprise, similar trend is observed in the cycleability plots with LCL electrolyte (shown in Figure S12(a)). Changing the salt to LiTFSI yielded similar results (Figure S12(b)). In case of LiPF_6 , the reaction with the water molecules should have caused a LiF layer to form over the materials and add impedance. However, LiClO_4 and LiTFSI are relatively stable salts with water, and shouldn't form any decomposed layer like LiF over the electrode and add impedance. Therefore, it can be safe to assume for the time being that the loss of water molecules may not have much effect on the degradation in the cycling behavior of the material.

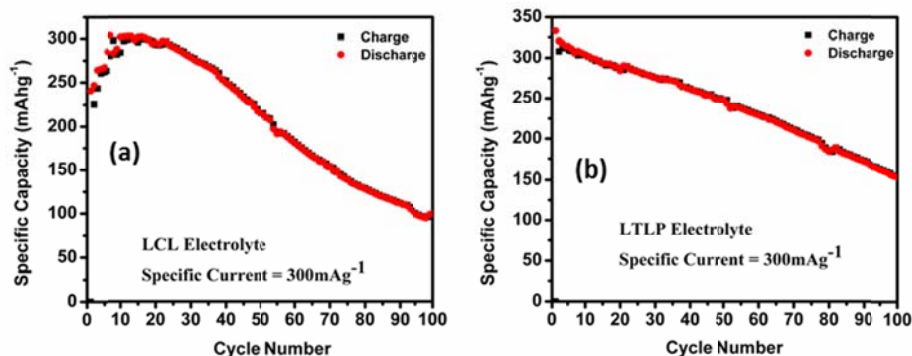


Figure S13: Cycleability plots for as-prepared electrodes with (a) LCL and (b) LTLP electrolytes, at same specific current.

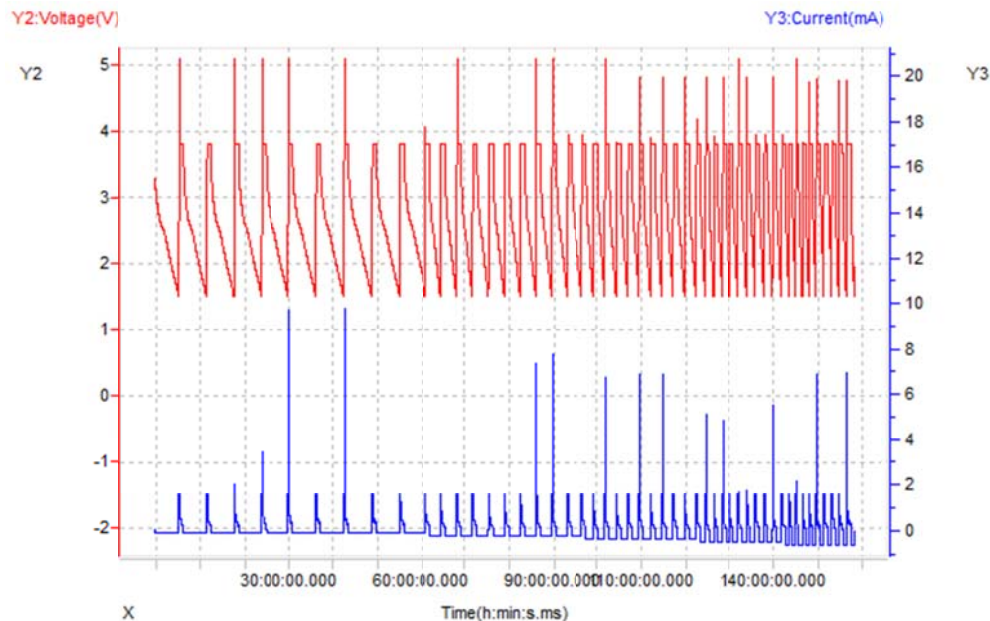


Figure S14: Raw Results from the battery tester, indicating the current spikes happening in some of the cycles, when the tester transitions from CC mode to CV mode.

S.3.9. KFM Topography and Surface Potential Maps

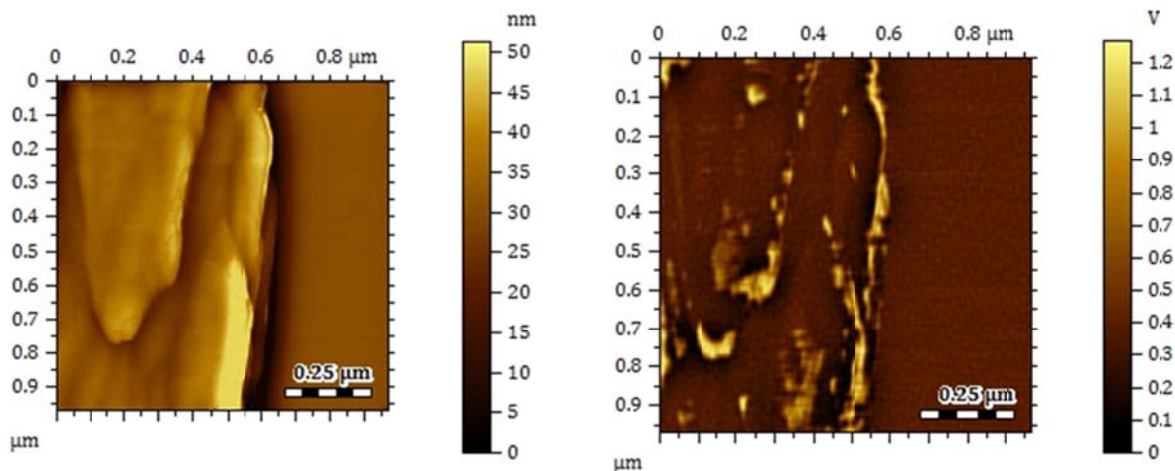


Figure S15: KFM Topography and Surface Potential maps obtained from the as-prepared particles, indicating the presence of high surface potential regions along the edges of the particles.

S.3.10. Comparison table for the electrochemical results for Kazakhstanite phase with the literature reported results

Table S5: Comparison table for the present work with several reported results in the literature, in terms of cycleability. It is to be noted that the materials under consideration are all vanadium based compounds since the solubility limit approach can also be extended to other vanadium containing compounds, to address the issue of poor cycleability.

Material under consideration	Method of synthesis	Year of Publication	Working potential window along with specific capacity	Cycleability reported	Rough estimation of the time taken to complete the cycleability based on the published results (hrs)	Ref.
$\text{Li}_{1.1}\text{V}_3\text{O}_8$	Freeze dried gel followed by calcination	2005	2.0V – 3.7V ~300mAhg ⁻¹ @ C/20 rate	30 cycles @ C/20 rate ~66% specific capacity loss (Vanadium dissolution reported)	~800	27
Lithium Decavanadate molecular clusters	Wet chemical synthesis	2020	1.5 – 3.8 V ~300mAhg ⁻¹ @ 50mA g ⁻¹	10 cycles @ 50mA g ⁻¹ ~93% specific capacity loss (Vanadium dissolution reported)	Estimation cannot be made	28
Ca ²⁺ functionalized dodecavanadate molecular clusters	Wet chemical synthesis	2020	2.0 - 4.0V ~60mAhg ⁻¹ @ 50mA g ⁻¹	10 cycles @ 50mA g ⁻¹ ~66% specific capacity loss (Vanadium dissolution reported)	Estimation cannot be made	29
FeVO @C composites (Kazakhstanite phase and Activated carbon)	Wet chemical synthesis	2020	1.5V – 4.0V ~ 90mAhg ⁻¹ @ 100mA g ⁻¹	2000 cycles @ 1A g ⁻¹ ~37% specific capacity loss	~280	30
Iron Vanadate (FVO) nanowire array on Ti Foil	Ion exchange with Na ₅ V ₁₂ O ₃₂	2019	0.0 - 3.0V ~1200mAh g ⁻¹ @ 300mA g ⁻¹ 2.0 - 4.0V ~223mAhg ⁻¹ @ 150mA g ⁻¹	100 cycles @ 300mA g ⁻¹ ~13% specific capacity loss in 0-3.0V potential window. 50 cycles @ 150mA g ⁻¹ ~8.7% specific capacity loss on 2.0-4.0V potential window.	~750 ~150	31
Urchin type Hollow porous VO ₂	Hydrothermal synthesis	2019	2.0 - 4.0V ~300mAhg ⁻¹ @ 0.2C	200 cycles @ 3C rate ~8% specific capacity loss	~ 133	32

			rate			
Layered Kazakhstanite phase Fe-V-O nanosheets	Water bath method	2018	1.5V - 4.0V 350mAhg ⁻¹ @ 100mAg ⁻¹	2000 cycles @10 Ag ⁻¹ ~16.7% specific capacity loss	~60	33
Fe _x V ₂ O ₅ nanorods	Sol-Gel method	2017	2.0 - 4.0V ~275mAhg ⁻¹ (2 nd Cycle)@ 100mAg ⁻¹ for 0.15- FeV ₂ O ₅	50 cycles @ 1 Ag ⁻¹ ~ 18% specific capacity loss	~ 50	34
Nanoflakes assembled 3D hollow porous V ₂ O ₅	Solvothermal reaction followed by high temperature calcination	2014	2.0V - 4.0V ~283mAhg ⁻¹ @ 100mAg ⁻¹	60 cycles @ 100mAg ⁻¹ ~23% specific capacity loss	~300	35
Fe-VO _x Nanotubes	Wet chemical synthesis of V ₂ O ₅ .nH ₂ O followed by cationic exchange	2012	1.5V – 4.0V ~300mAhg ⁻¹ @ 100mAg ⁻¹ 1.5V – 4.0V ~311mAhg ⁻¹ @ 50mAg ⁻¹	50 cycles @ 100mAg ⁻¹ ~50% specific capacity loss 50 cycles @ 50mAg ⁻¹ ~43% specific capacity loss	~190 ~500	36
Nanocrystalline Ag ₂ V ₄ O ₁₁	Room temperature wet chemical synthesis	2010	1.5V – 3.8V ~300mAhg ⁻¹ @ 2C rate	30 cycles @ 2C rate ~66% specific capacity loss	~30	37
Several Iron Vanadates along with their related compounds	Several techniques which are different for different compositions	2007	Best Result: 2.0V - 3.5V ~205mAhg ⁻¹ @ C/5 rate	<25 Cycles @ C/5 rate No apparent loss	<250	38
Layered Kazakhstanite phase nanosheets	Wet chemical synthesis	-	1.5V - 3.8V ~300mAhg⁻¹ @ 100mAg⁻¹	500 cycles @100mAg⁻¹ ~20 % specific capacity loss in last 440 cycles (Vanadium dissolution reported)	~2200	This Work

S.3.11. Post cycling identification of dissolution process

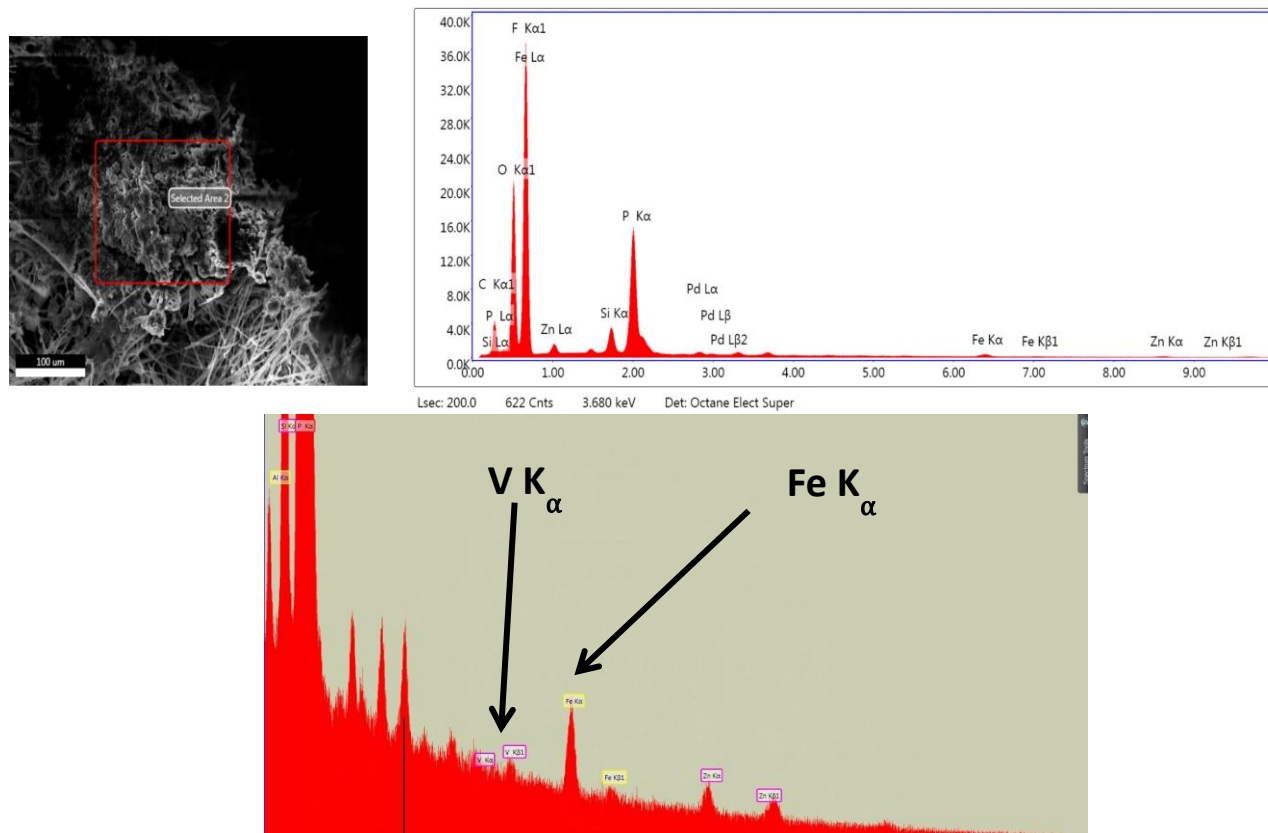


Figure S16: EDS spectrum collected from the separators cycled with the electrochemical cell containing EE electrolyte. The separators show significant amount of detectable Fe and V leaching out of the Kazakhstanite phase.

Element	Weight %	Atomic %	Error %
C K	14.33	22.13	10.01
O K	20.76	24.08	7.26
F K	41.52	40.55	7.72
Na K	0.24	0.19	90.48
Al K	0.45	0.31	9.34
Si K	2.4	1.58	4.4
P K	16.78	10.05	3.01
V K	0.15	0.05	38.71
Fe K	1.69	0.56	10.63

Table S6: Quantification table for the elements detected in separators, cycled with the electrochemical cell containing EE electrolyte, using EDS

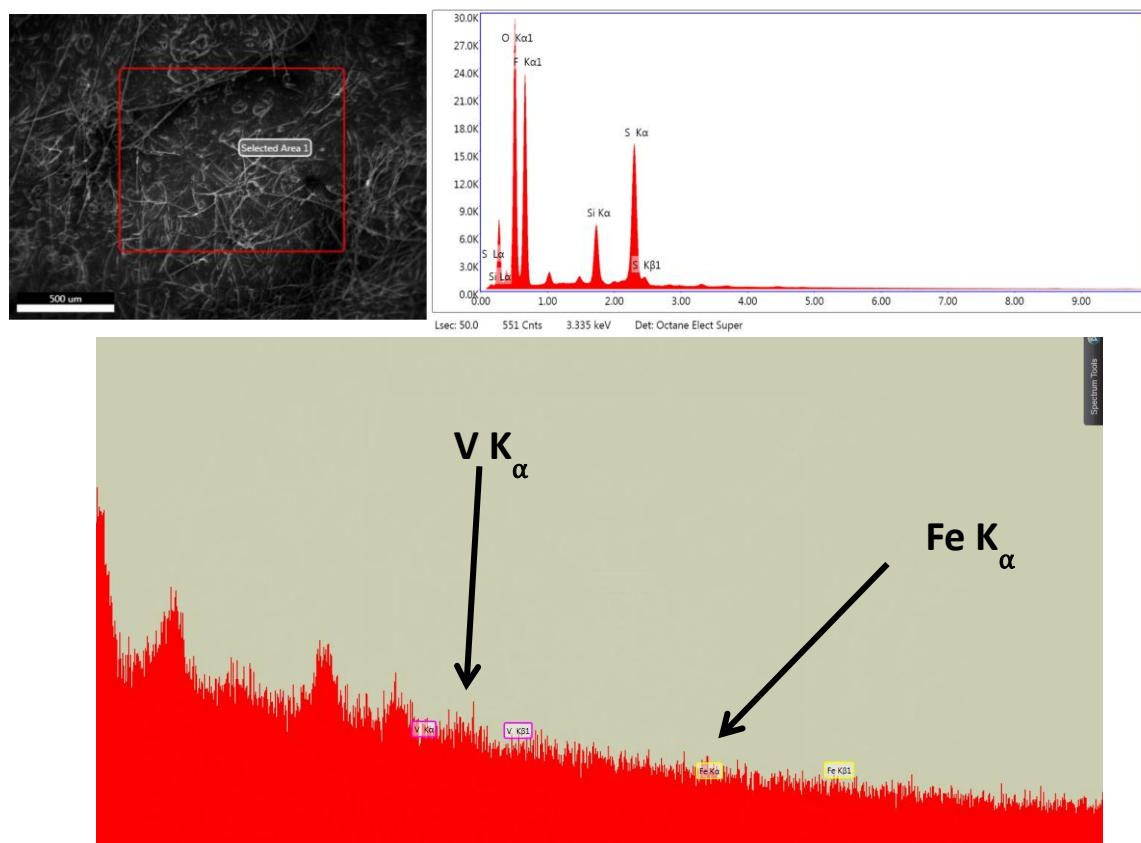


Figure S17: EDS spectrum collected from the separators cycled with the electrochemical cell containing EL4 electrolyte. The Fe and V are almost undetectable in the separators.

Element	Weight %	Atomic %	Error %
O K	31.73	39.98	6.69
F K	37.44	39.73	8.33
Na K	1.62	1.42	11.79
Si K	6.32	4.53	3.74
S K	22.67	14.25	2.57
V K	0.12	0.05	57.85
Fe K	0.09	0.03	59.9

Table S7: Quantification table for the elements detected in separators, cycled with the electrochemical cell containing EL4 electrolyte, using EDS.

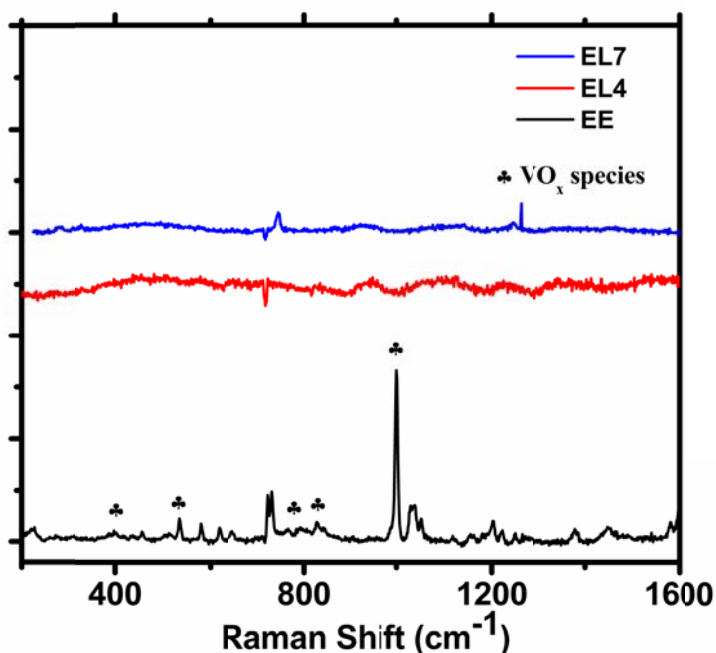


Figure S18: Raman Spectra of the cycled lithium foil counter electrodes cycled with the different electrolytes (EE, EL4, EL7).

S.3.12. Preliminary Full Cell Characterization with Lithiated Graphite:

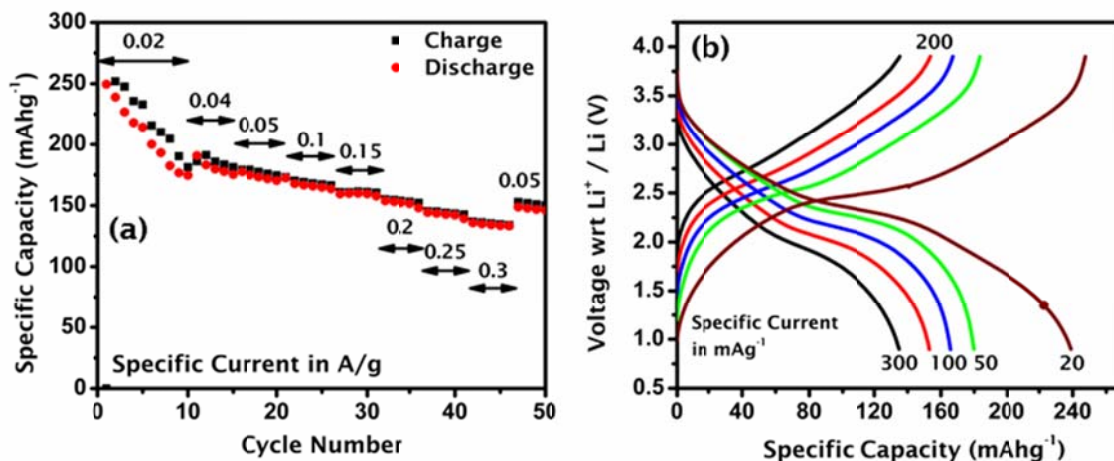


Figure S19: (a) Rate-cum cycleability plot for a full cell of Kazakhstanite with lithiated graphite and EL7 electrolyte. (b) Charge-Discharge Profile of the full cell constructed at the different specific current.

Figure S19 shows the preliminary full cell characteristics of the Kazakhstanite phase with EL7 electrolyte and lithiated graphite. It is observed that the full cell show good rate capability and good cycleability at higher specific current. At lower specific current, we observe that there is large drop in specific capacity. We believe this is due to imbalanced mass loading, which affected the total amount of cycleable lithium ions. This is further demonstrated in the charge-discharge profile, where the plateau below 2.0V for the Kazakhstanite is no more present. This is due to limited amount of lithiated anode present, which started operating at its tail region ($>0.3\text{V}$ wrt Li^+/Li), rather than operating at the plateau regions ($<0.3\text{V}$ wrt Li^+/Li). Further studies are underway to create a mass balanced full cell, and also eliminate the need for lithiated anodes.

Section S4: Impact of the local electrolyte structure and the electrochemical characteristics of the passivation layers (over Lithium counter electrode) on the improved cycleability using superconcentrated electrolytes

S.4.1. Physico-chemical property evaluation of different electrolyte systems under study

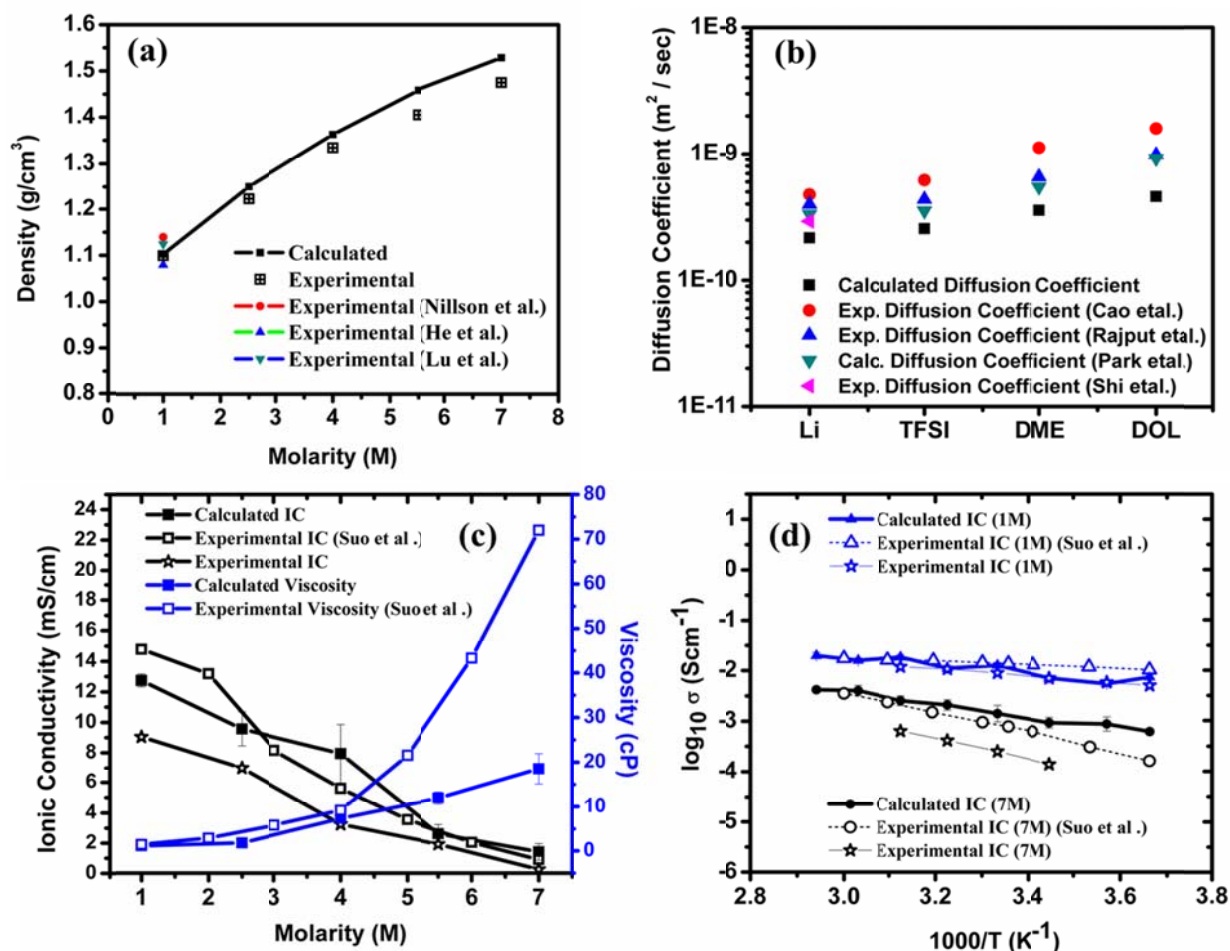


Figure S20: (a) The calculated and experimental densities of the various electrolyte compositions which are undertaken for the simulation studies.³⁹⁻⁴¹ (b) The calculated diffusion coefficients of the various ionic and solvent species in EL1 composition, along with their comparison with reported values in the literature.⁴²⁻⁴⁵ (c) The calculated ionic conductivity and viscosity of the various electrolyte compositions tested for the simulation studies, along with a comparison with the experimental values.⁴⁶ (d) The temperature-dependent ionic conductivity

values for the EL1 (relatively dilute) and EL7 (superconcentrated) electrolytes [experimental and calculated].⁴⁶

Figure S20 shows the calculated density, ionic conductivity and viscosity of the different simulated electrolyte compositions. An increase in density is observed as the salt concentration increases from 1M to 7M. Since EL1 is a frequently studied electrolyte composition as a part of Li-S batteries, it is important that the physico-chemical properties calculated from our MD model matches well with the values reported in the literature. As shown in Figure S20(a), the calculated density for EL1 matches well with some of the experimental results reported in the literature with a deviation <2%.^{39-41, 47} The deviations between the measured and calculated densities for other compositions are also observed to be within 3%. This indicates that the force-field parameters used in the simulations should correctly predict the ion-ion and ion-solvent interactions. The densities calculated for pure DOL and pure DME are also observed to match well with the literature reported experimental values, as shown in Table S8. The self-diffusion coefficient of Li⁺, TFSI, DOL, and DME for EL1, presented in Figure S20(b), is calculated from the intercept of a linear fit of MSD vs. time in log-log scale. The slope of the linear fit, which indicates the power dependency of MSD with time, is close to 1 for all the cases. This indicates that the self-diffusion of the ions and solvent exhibit a Fickian-type behavior. The calculated self-diffusion coefficients and the values reported in the literature are also observed to be of the same order of magnitude.⁴²⁻⁴⁵ The large deviation in the experimentally reported values makes it difficult to correctly compare our calculated values with the experimental ones. Furthermore, non-polarizable force-fields are known to generate deviations of several orders of magnitudes, which are not observed in our case due to appropriate charge scaling.⁴⁸⁻⁵² For eg. Rajput et al. have also calculated self-diffusion coefficients of Li⁺, TFSI, DOL, and DME, which are over 1 order of magnitude different from the experimentally obtained values.⁴⁴ The complete dataset for the calculated diffusion coefficients of the ions and solvents for the different concentrations of salt (LiTFSI) in solvent (DOL: DME = 1:1 v:v) is presented in Table S9. The calculated ionic conductivity and shear viscosity of the different compositions of the electrolyte are shown in Figure S20(c). For the ionic conductivity, the Nernst-Einstein equation is not appropriate since it is derived for an infinitely dilute electrolyte system, wherein the ion-ion interactions are negligible. Therefore, a form of the ionic conductivity which accounts for the ion-ion interactions has been used to calculate the values for the concentrated electrolytes.²¹ The ionic conductivity is observed to decrease as the concentration of LiTFSI in the electrolytes increases, which indicates that the strong ion-ion interactions hinder the movement of the ionic clusters in the concentrated electrolytes. This is also indicated by the reduced self-diffusion coefficient of the ions and the solvent molecules as the concentration of LiTFSI is increased (Table S9). As the concentration of LiTFSI is increased, a subdiffusive behavior is observed for the ions and the solvent molecules. The increase in the calculated shear viscosity also supports this reasoning. Suo et al. have reported a systematic experimental estimations of ionic conductivity and viscosity of electrolytes with varying concentration of LiTFSI (ranging from 1M-7M).⁴⁶ These values are plotted against our calculated and experimentally obtained results for comparison in Figures

S20(c) and (d). While the ionic conductivity and shear viscosity follow the same trend as reported by Suo et al., a large deviation between the experimental and calculated values is observed for the shear viscosity. We believe that this discrepancy is due to the use of non-polarizable force-field, where our partial charge scaling factor should ideally be modified depending on the concentration of LiTFSI. As the concentration of LiTFSI in the system is increased, the effective screening of the ions from the solvent molecules is reduced due to the sheer number of the ions introduced into the system. Therefore, the partial charge scaling factor should be larger at higher concentrations. The calculated and the observed values are nearly equivalent for the compositions EL1-EL4. The deviations begin to appear when the concentration of LiTFSI is increased beyond 4M. Nevertheless, the calculated values do not differ significantly from the experimental ones. Therefore, the simulation model under study is suitable to gain a deeper understanding of the behavior of such concentrated electrolyte systems.

Table S8: Calculated Density of pure DOL and DME post equilibration

System	Calculated Density (g/cc)	Experimental Density (g/cc) from Literature
Pure DOL	1.0675 ± 0.0028	1.06
Pure DME	0.9084 ± 0.002	0.868

Table S9: Calculated Self Diffusion Coefficients of the ions and solvents for the different concentrations of salt (LiTFSI) in solvent (DOL: DME = 1:1 v:v)

Concentration (M)	Self Diff. Coeff of Li ⁺ (m ² sec ⁻¹), time exponent α	Self Diff. Coeff of TFSI ⁻ (m ² sec ⁻¹), time exponent α	Self Diff. Coeff of DOL (m ² sec ⁻¹), time exponent α	Self Diff. Coeff of DME (m ² sec ⁻¹), time exponent α	Behavior
1	2.16E-10, 1.0032	2.56E-10, 0.9008	4.60E-10, 0.9657	3.57E-10, 0.9373	Brownian
2.5	1.40E-10, 0.9654	1.69E-10, 0.9027	3.19E-10, 0.9675	1.78E-10, 0.8861	Nearly Brownian
4	4.75E-11, 0.9192	7.47E-11, 0.82665	9.91E-11, 0.887	7.45E-11, 0.7805	Sub-Diffusive
5.5	1.94E-11, 0.825	3.69E-11, 0.6884	3.53E-11, 0.7476	4.11E-11, 0.6354	Sub-Diffusive
7	1.18E-11, 0.70509	2.37E-11, 0.595	2.06E-11, 0.6137	2.80E-11, 0.53	Sub-Diffusive

S.4.2. Ion-dynamics of V^{3+} -TFSI $^{-}$ ion pair with different cutoff radius

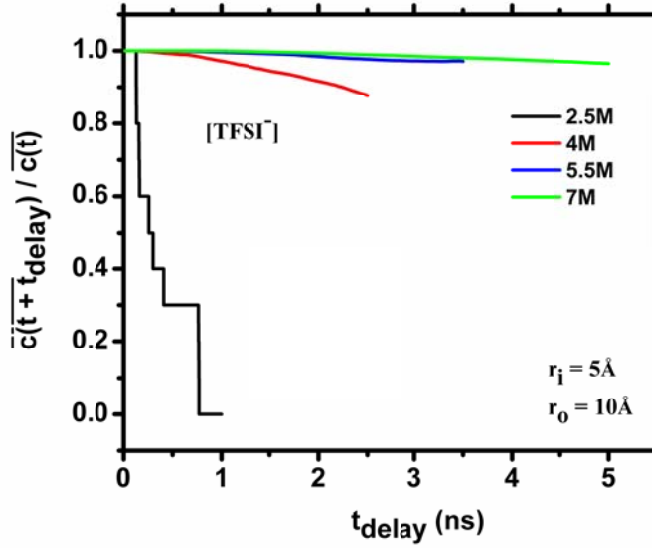


Figure S21: Fraction of active clusters which did not undergo any deletion event against time according to the equation (1) for V^{3+} -TFSI $^{-}$ ion pairs, at different concentrations ($r_1 = 5 \text{ \AA}$).

S.4.3. Lithium-ion diffusion mechanism through the passivation layers formed over the lithium counter electrode

We present a mathematical derivation for the diffusion of Li-ions through this bilayer. We assume the thickness of the passivation layer to be L_1 and thickness of the SEI layer to be L_2 . Let the diffusivities through the passivation layer be D_1 , and through the SEI be D_2 . During the migration of lithium-ions through these layers, it is assumed that there are no changes in their thickness. Also the diffusivities are assumed to be constant throughout the thickness. The transport properties of Li-ion through these layers will follow the Fick's Second law of diffusion, when a small perturbation is introduced over the steady state condition.

$$\frac{\partial c_1}{\partial t} = D_1 \frac{\partial^2 c_1}{\partial x^2} \quad (0 < x < L_1);$$

$$\frac{\partial c_2}{\partial t} = D_2 \frac{\partial^2 c_2}{\partial x^2} \quad (L_1 < x < L_1 + L_2) \quad (1)$$

Applying Laplace transformation to equation set (1) to convert them into linear differential equations:

$$\begin{aligned}
-c_1(x, 0) + s\hat{c}_1(x, s) &= D_1 \frac{d^2\hat{c}_1(x, s)}{dx^2} ; \\
-c_2(x, 0) + s\hat{c}_2(x, s) &= D_2 \frac{d^2\hat{c}_2(x, s)}{dx^2}
\end{aligned} \tag{2}$$

where $c_1(x,0)$ and $c_2(x,0)$ are the steady state initial conditions before the perturbation was introduced. We introduce variables Δc_1 and Δc_2 , which are the difference between the instantaneous concentration values from their steady state values. Therefore, the equation set (2) can be re-written as:

$$\begin{aligned}
s\Delta\hat{c}_1(x, s) &= D_1 \frac{d^2\Delta\hat{c}_1(x, s)}{dx^2} ; \\
s\Delta\hat{c}_2(x, s) &= D_2 \frac{d^2\Delta\hat{c}_2(x, s)}{dx^2}
\end{aligned} \tag{3}$$

The characteristic solutions for the above linear differential equations are (no particular solution is there since constant = 0):

$$\begin{aligned}
\Delta\hat{c}_1(x, s) &= \alpha_1 \exp\left(\sqrt{\frac{s}{D_1}} x\right) + \alpha_2 \exp\left(-\sqrt{\frac{s}{D_1}} x\right) ; \\
\Delta\hat{c}_2(x, s) &= \beta_1 \exp\left(\sqrt{\frac{s}{D_2}} (x - L_1)\right) + \beta_2 \exp\left(-\sqrt{\frac{s}{D_2}} (x - L_1)\right)
\end{aligned} \tag{4}$$

The diffusion flux ΔJ in the Laplace space can be calculated by calculating the derivative of the equation set (4) and multiplying by appropriate pre-factor ($-D_1$ for $\Delta\hat{J}_1$ and $-D_2$ for $\Delta\hat{J}_2$).

$$\begin{aligned}
\Delta\hat{J}_1(x, s) &= -\sqrt{sD_1} \left[\alpha_1 \exp\left(\sqrt{\frac{s}{D_1}} x\right) - \alpha_2 \exp\left(-\sqrt{\frac{s}{D_1}} x\right) \right] ; \\
\Delta\hat{J}_2(x, s) &= -\sqrt{sD_2} \left[\beta_1 \exp\left(\sqrt{\frac{s}{D_2}} (x - L_1)\right) - \beta_2 \exp\left(-\sqrt{\frac{s}{D_2}} (x - L_1)\right) \right]
\end{aligned} \tag{5}$$

A matrix formulation can be constructed based on the ideation by Chen *et al.* and Diard *et al.* to represent the concentration and the diffusion flux at a certain point in space, with respect to another point (both points within the boundary).⁵³⁻⁵⁴

$$\begin{vmatrix} \Delta\hat{c}_1(x, s) \\ \Delta\hat{J}_1(x, s) \end{vmatrix} = \begin{vmatrix} \cosh\left(\sqrt{\frac{s}{D_1}} \delta\right) & \frac{\sinh\left(\sqrt{\frac{s}{D_1}} \delta\right)}{-\sqrt{sD_1}} \\ -\sqrt{sD_1} \sinh\left(\sqrt{\frac{s}{D_1}} \delta\right) & \cosh\left(\sqrt{\frac{s}{D_1}} \delta\right) \end{vmatrix} \begin{vmatrix} \Delta\hat{c}_1(x + \delta, s) \\ \Delta\hat{J}_1(x + \delta, s) \end{vmatrix} \tag{6}$$

Similarly, the matrix formulation for the region $L_1 < x < L_2$ can be written as

$$\begin{vmatrix} \Delta \hat{c}_2(x, s) \\ \Delta \hat{J}_2(x, s) \end{vmatrix} = \begin{vmatrix} \cosh\left(\sqrt{\frac{s}{D_2}} \delta\right) & \frac{\sinh\left(\sqrt{\frac{s}{D_2}} \delta\right)}{-\sqrt{sD_2}} \\ -\sqrt{sD_2} \sinh\left(\sqrt{\frac{s}{D_2}} \delta\right) & \cosh\left(\sqrt{\frac{s}{D_2}} \delta\right) \end{vmatrix} \begin{vmatrix} \Delta \hat{c}_2(x + \delta, s) \\ \Delta \hat{J}_2(x + \delta, s) \end{vmatrix} \quad (7)$$

Now, the diffusion impedance Z_{mt} is $(\partial E/\partial i)_{mt}$ which can be written as $(\partial E/\partial c)(\partial c/\partial J)(\partial J/\partial i)$ by chain rule. The terms $(\partial E/\partial c)$ and $(\partial J/\partial i)$ can be clubbed as a constant k . These values can be obtained by plugging in the appropriate expressions for dependence of electrochemical potential with concentration (can be calculated by estimating the SOC of the material), and dependence of current density with current. Therefore diffusion impedance is directly proportional to $(\partial c/\partial J)$, which can now be obtained from the equations (6) and (7). For $x=0$ and $\delta=L_1$ (the end points of the passivation layer) in equation (6), and $x=L_1$ and $\delta=L_2$ (the end points of the SEI layer) in equation (7), we obtain

$$\begin{vmatrix} \Delta \hat{c}_1(0, s) \\ \Delta \hat{J}_1(0, s) \end{vmatrix} = \begin{vmatrix} \cosh\left(\sqrt{\frac{s}{D_1}} L_1\right) & \frac{\sinh\left(\sqrt{\frac{s}{D_1}} L_1\right)}{-\sqrt{sD_1}} \\ -\sqrt{sD_1} \sinh\left(\sqrt{\frac{s}{D_1}} L_1\right) & \cosh\left(\sqrt{\frac{s}{D_1}} L_1\right) \end{vmatrix} \begin{vmatrix} \Delta \hat{c}_1(L_1, s) \\ \Delta \hat{J}_1(L_1, s) \end{vmatrix};$$

$$\begin{vmatrix} \Delta \hat{c}_2(L_1, s) \\ \Delta \hat{J}_2(L_1, s) \end{vmatrix} = \begin{vmatrix} \cosh\left(\sqrt{\frac{s}{D_2}} L_2\right) & \frac{\sinh\left(\sqrt{\frac{s}{D_2}} L_2\right)}{-\sqrt{sD_2}} \\ -\sqrt{sD_2} \sinh\left(\sqrt{\frac{s}{D_2}} L_2\right) & \cosh\left(\sqrt{\frac{s}{D_2}} L_2\right) \end{vmatrix} \begin{vmatrix} \Delta \hat{c}_2(L_1 + L_2, s) \\ \Delta \hat{J}_2(L_1 + L_2, s) \end{vmatrix} \quad (8)$$

In order to maintain the conditions for continuity and conditions for no charge accumulation at the interface, we have $\Delta \hat{c}_1(L_1, s) = \Delta \hat{c}_2(L_1, s)$ and $\Delta \hat{J}_1(L_1, s) = \Delta \hat{J}_2(L_1, s)$. We introduce three variables which are $m = -D_1/L_1$, $\Lambda = \sqrt{D_1/D_2}$ and $\lambda = \sqrt{D_1/D_2}(L_2/L_1)$ to simplify the matrix, and represent $\sqrt{s/D_1} L_1$ as u . Therefore, the two equations in the set (8) can be combined to obtain

$$\begin{vmatrix} \Delta \hat{c}_1(0, s) \\ \Delta \hat{J}_1(0, s) \end{vmatrix} = \begin{vmatrix} a_{11} & a_{12} \\ a_{21} & a_{22} \end{vmatrix} \begin{vmatrix} \Delta \hat{c}_2(L_1 + L_2, s) \\ \Delta \hat{J}_2(L_1 + L_2, s) \end{vmatrix} \quad (9)$$

where

$$a_{11} = \cosh(u) \cosh(\lambda u) + \frac{1}{\Lambda} \sinh(u) \sinh(\lambda u)$$

$$a_{12} = \frac{\cosh(u) \sinh(\lambda u)}{-\sqrt{sD_1}} + \frac{\sinh(u) \cosh(\lambda u)}{-\sqrt{sD_2}}$$

$$a_{21} = -\sqrt{sD_1} \sinh(u) \cosh(\lambda u) - \sqrt{sD_2} \cosh(u) \sinh(\lambda u)$$

$$a_{22} = \cosh(u) \cosh(\lambda u) + \Lambda \sinh(u) \sinh(\lambda u)$$

Z_{mt} is directly proportional to $\Delta\hat{c}_1(0, s) / \Delta\hat{J}_1(0, s)$, which can now be effectively calculated by putting the appropriate expression for $\Delta\hat{c}_2$ and $\Delta\hat{J}_2$ in equation (9) based on the boundary conditions present in the system under consideration. Since lithium foil surface exists at $x=L_1+L_2$, it acts as an infinite source of the diffusing lithium ions. Thus, $\Delta\hat{c}_2(L_1+L_2, s) = 0$. Therefore, the expression for Z_{mt} can be written as

$$Z_{mt} \propto \frac{\Delta\hat{c}_1(0,s)}{\Delta\hat{J}_1(0,s)} = \frac{a_{12}}{a_{22}} = \frac{\Lambda \tanh(\lambda u) + \tanh(u)}{mu[\Lambda \tanh(u) \tanh(\lambda u) + 1]} \quad (10)$$

By putting complex number $s = j\omega$ in the above equation (10), the net complex impedance due to bilayer diffusion can be obtained. This expression is incorporated into the ZSimpwin framework as the J symbol.

Electrolyte	Q (Y_0, n) [S- sec ⁿ /cm ² , dim.less]	R _{CT(Fe)} [ohm- cm ²]	R _{elec} [ohm- cm ²]	Q (Y_0, n) [S- sec ⁿ /cm ²]	J ($Y_0, \omega_0, \Lambda, \lambda$) [S- sec ⁿ /cm ² , sec ⁻¹ , dim.less, dim.less]
EL7	5.617E-6, 0.6506	131.1	184.4	0.00157, 0.5825	0.001351, 152.3, 0.05876, 72.59
LTLF	2.648E-6, 0.8802	44.72	11.31	0.0006098, 0.4683	0.04464, 45.12, 4.775, 44.95

Table S10: Equivalent Circuit Parameters after fitting the experimental EIS spectrum for EL7 and LTLF Electrolytes, after 100 cycles of cycling of the Kazakhstanite electrodes.

Section S5: Structural Characteristics and addition electrochemical results for commercial V_2O_5 , as-synthesized LiV_3O_8 , and commercial $LiMn_2O_4$

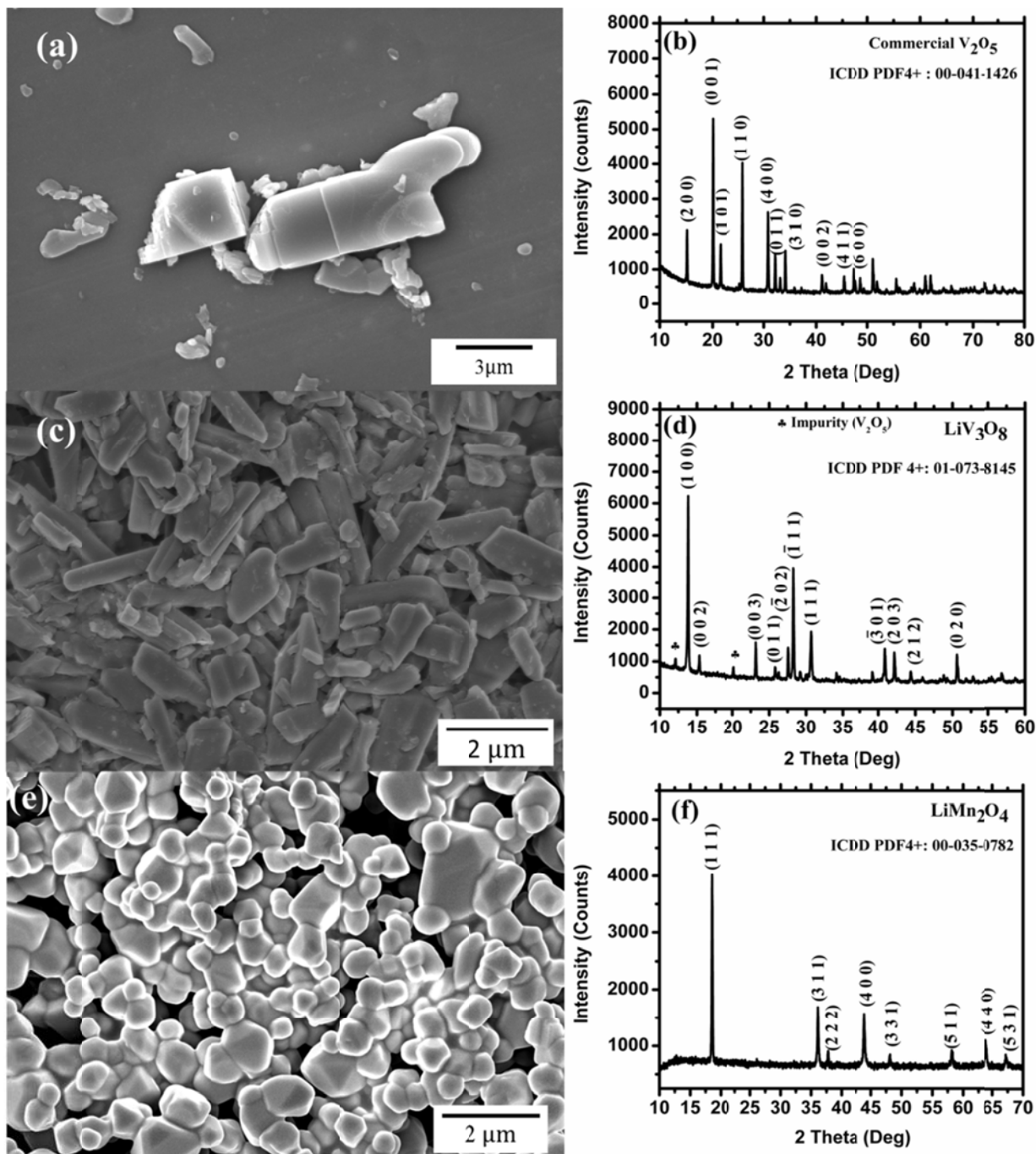


Figure S22: Microstructural (Scanning electron micrographs) and Structural (X-ray diffractograms) features of (a) Commercial V_2O_5 , (b) As-synthesized LiV_3O_8 , (c) Commercial $LiMn_2O_4$, which have been used to experimentally validate the theoretical results.

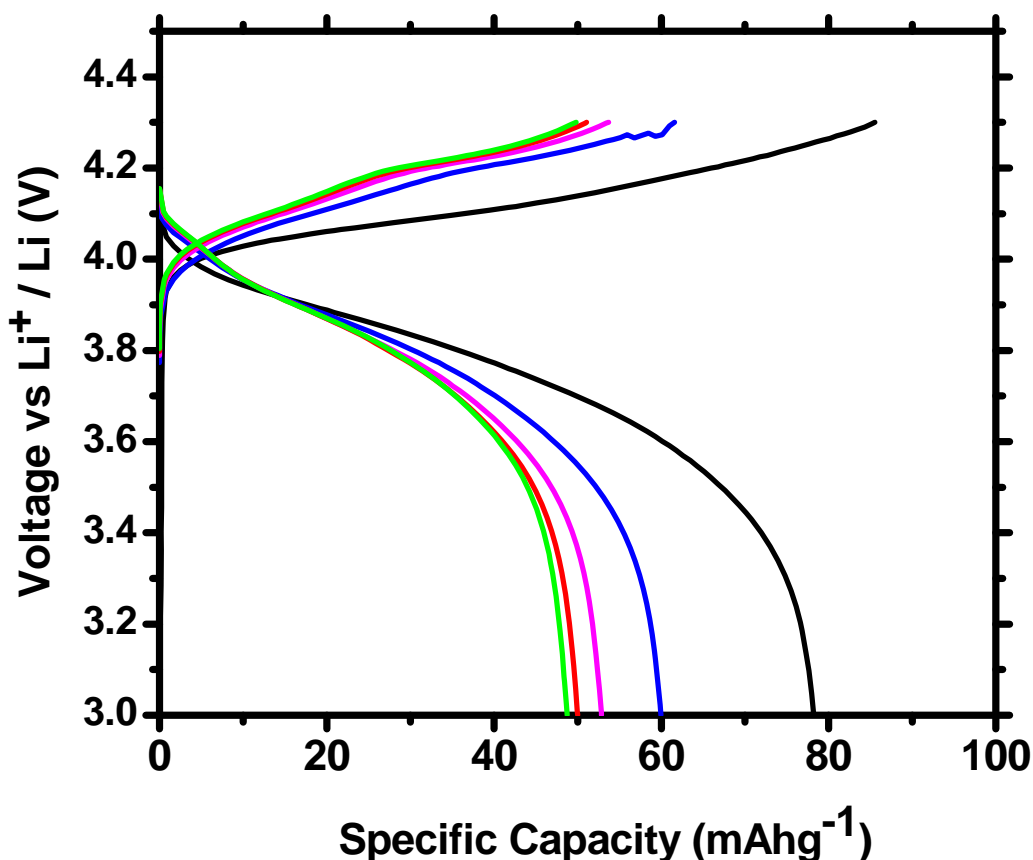


Figure S23: Charge-Discharge Profile of the commercial LiMn_2O_4 electrodes tested with EL7 electrolyte (First five cycles). The specific capacity of the electrodes obtained with EL7 electrolyte are very low due to the high viscosity of the EL7 electrolyte, making it unattractive to use as a potential electrolyte for LiMn_2O_4 cathode.

References

1. Pan, A.; Liu, J.; Zhang, J.-G.; Cao, G.; Xu, W.; Nie, Z.; Jie, X.; Choi, D.; Arey, B. W.; Wang, C.; Liang, S., Template free synthesis of LiV_3O_8 nanorods as a cathode material for high-rate secondary lithium batteries. *Journal of Materials Chemistry* **2011**, *21* (4), 1153-1161.
2. Toby, B. H.; Von Dreele, R. B., GSAS-II: the genesis of a modern open-source all purpose crystallography software package. *Journal of Applied Crystallography* **2013**, *46* (2), 544-549.
3. Schneider, C. A.; Rasband, W. S.; Eliceiri, K. W., NIH Image to ImageJ: 25 years of image analysis. *Nature Methods* **2012**, *9* (7), 671-675.

4. Wojdyr, M., Fityk: a general-purpose peak fitting program. *Journal of Applied Crystallography* **2010**, *43* (5-1), 1126-1128.
5. Das, D.; Mitra, A.; Jena, S.; Majumder, S. B.; Basu, R. N., Electrophoretically Deposited ZnFe₂O₄-Carbon Black Porous Film as a Superior Negative Electrode for Lithium-Ion Battery. *ACS Sustainable Chemistry & Engineering* **2018**, *6* (12), 17000-17010.
6. Ray, U.; Das, D.; Jena, S.; Mitra, A.; Das, K.; Majumder, S. B.; Das, S., Electrophoretically deposited NiSb₂O₆-carbon black composite film as a potential anode for sodium-ion battery. *Surface and Coatings Technology* **2021**, *408*, 126787.
7. Yeum, B., ZSimpWin 3.21, EChem Software. *Ann Arbor, Michigan, USA (1999-2005)* **1999**.
8. Plimpton, S. In *Particle-Mesh Ewald and rRESPA for Parallel Molecular Dynamics Simulations*, Citeseer.
9. Plimpton, S., Fast parallel algorithms for short-range molecular dynamics. *Journal of computational physics* **1995**, *117* (1), 1-19.
10. Martínez, L.; Andrade, R.; Birgin, E. G.; Martínez, J. M., PACKMOL: a package for building initial configurations for molecular dynamics simulations. *Journal of computational chemistry* **2009**, *30* (13), 2157-2164.
11. Hanwell, M. D.; Curtis, D. E.; Lonie, D. C.; Vandermeersch, T.; Zurek, E.; Hutchison, G. R., Avogadro: an advanced semantic chemical editor, visualization, and analysis platform. *Journal of cheminformatics* **2012**, *4* (1), 17.
12. Jewett, A. I.; Zhuang, Z.; Shea, J.-E., Moltemplate a coarse-grained model assembly tool. *Biophysical Journal* **2013**, *104* (2), 169a.
13. Jorgensen, W. L.; Maxwell, D. S.; Tirado-Rives, J., Development and testing of the OPLS all-atom force field on conformational energetics and properties of organic liquids. *Journal of the American Chemical Society* **1996**, *118* (45), 11225-11236.
14. Canongia Lopes, J. N.; Pádua, A. A., Molecular force field for ionic liquids composed of triflate or bistriflylimide anions. *The Journal of Physical Chemistry B* **2004**, *108* (43), 16893-16898.
15. MacKerell, A. D.; Bashford, D.; Bellott, M.; Dunbrack, R. L.; Evanseck, J. D.; Field, M. J.; Fischer, S.; Gao, J.; Guo, H.; Ha, S.; Joseph-McCarthy, D.; Kuchnir, L.; Kuczera, K.; Lau, F. T. K.; Mattos, C.; Michnick, S.; Ngo, T.; Nguyen, D. T.; Prodhom, B.; Reiher, W. E.; Roux, B.; Schlenkrich, M.; Smith, J. C.; Stote, R.; Straub, J.; Watanabe, M.; Wiórkiewicz-Kuczera, J.; Yin, D.; Karplus, M., All-Atom Empirical Potential for Molecular Modeling and Dynamics Studies of Proteins. *The Journal of Physical Chemistry B* **1998**, *102* (18), 3586-3616.
16. Pluhařová, E.; Fischer, H. E.; Mason, P. E.; Jungwirth, P., Hydration of the chloride ion in concentrated aqueous solutions using neutron scattering and molecular dynamics. *Molecular Physics* **2014**, *112* (9-10), 1230-1240.
17. Gupta, S.; Wai, N.; Lim, T. M.; Mushrif, S. H., Force-field parameters for vanadium ions (+2, +3, +4, +5) to investigate their interactions within the vanadium redox flow battery electrolyte solution. *Journal of Molecular Liquids* **2016**, *215*, 596-602.
18. Raček, T.; Schindler, O.; Toušek, D.; Horský, V.; Berka, K.; Koča, J.; Svobodová, R., Atomic Charge Calculator II: web-based tool for the calculation of partial atomic charges. *Nucleic Acids Research* **2020**, *48* (W1), W591-W596.
19. Chaudhari, M. I.; Nair, J. R.; Pratt, L. R.; Soto, F. A.; Balbuena, P. B.; Rempe, S. B., Scaling Atomic Partial Charges of Carbonate Solvents for Lithium Ion Solvation and Diffusion. *Journal of Chemical Theory and Computation* **2016**, *12* (12), 5709-5718.

20. Leontyev, I. V.; Stuchebrukhov, A. A., Electronic continuum model for molecular dynamics simulations of biological molecules. *Journal of chemical theory and computation* **2010**, *6* (5), 1498-1508.
21. France-Lanord, A.; Grossman, J. C., Correlations from Ion Pairing and the Nernst-Einstein Equation. *Physical Review Letters* **2019**, *122* (13), 136001.
22. Müller-Plathe, F., Reversing the perturbation in nonequilibrium molecular dynamics: An easy way to calculate the shear viscosity of fluids. *Physical Review E* **1999**, *59* (5), 4894.
23. Mezei, M., The finite difference thermodynamic integration, tested on calculating the hydration free energy difference between acetone and dimethylamine in water. *The Journal of chemical physics* **1987**, *86* (12), 7084-7088.
24. Pearlman, D. A., A comparison of alternative approaches to free energy calculations. *The Journal of Physical Chemistry* **1994**, *98* (5), 1487-1493.
25. Baddour-Hadjean, R.; Pereira-Ramos, J. P.; Navone, C.; Smirnov, M., Raman Microspectrometry Study of Electrochemical Lithium Intercalation into Sputtered Crystalline V2O5 Thin Films. *Chemistry of Materials* **2008**, *20* (5), 1916-1923.
26. Criddle, A. J.; Stanley, C. J., *Quantitative data file for ore minerals*. Springer Science & Business Media: **2012**.
27. Jouanneau, S.; La Salle, A. L. G.; Verbaere, A.; Guyomard, D., The origin of capacity fading upon lithium cycling in Li1.1V3O8. *Journal of the Electrochemical Society* **2005**, *152* (8), A1660.
28. Greiner, S.; Anjass, M. H.; Fichtner, M.; Streb, C., Solid-state-stabilization of molecular vanadium oxides for reversible electrochemical charge storage. *Inorganic Chemistry Frontiers* **2020**, *7* (1), 134-139.
29. Greiner, S.; Schwarz, B.; Ringenberg, M.; Dürr, M.; Ivanovic-Burmazovic, I.; Fichtner, M.; Anjass, M.; Streb, C., Redox-inactive ions control the redox-activity of molecular vanadium oxides. *Chemical Science* **2020**, *11* (17), 4450-4455.
30. Lu, R.; Ren, X.; Zhan, C.; Wang, C.; Lv, R.; Shen, W.; Kang, F.; Huang, Z.-H., Facile synthesis of FeVO@C materials as high-performance composite cathode for lithium-ion hybrid capacitor. *Journal of Alloys and Compounds* **2020**, *835*, 155398.
31. Hua, K.; Fang, D.; Bao, R.; You, X.; Tao, J.; Li, C.; Liu, Y.; Luo, Z.; Yi, J.; Shu, Y.; Sun, B., Porous iron vanadate nanowire arrays on Ti foil as a high-performance lithium-ion battery. *Applied Surface Science* **2019**, *465*, 1047-1054.
32. Lim, S.-Y., Urchin-type hollow porous structured vanadium oxide nanorod for one-dimensional lithium ion battery cathodes. *Solid State Sciences* **2019**, *96*, 105949.
33. Wei, Q.; Wang, Q.; Li, Q.; An, Q.; Zhao, Y.; Peng, Z.; Jiang, Y.; Tan, S.; Yan, M.; Mai, L., Pseudocapacitive layered iron vanadate nanosheets cathode for ultrahigh-rate lithium ion storage. *Nano Energy* **2018**, *47*, 294-300.
34. Liang, X.; Gao, G.; Liu, Y.; Zhang, T.; Wu, G., Synthesis and characterization of Fe-doped vanadium oxide nanorods and their electrochemical performance. *Journal of Alloys and Compounds* **2017**, *715*, 374-383.
35. Mai, L.; An, Q.; Wei, Q.; Fei, J.; Zhang, P.; Xu, X.; Zhao, Y.; Yan, M.; Wen, W.; Xu, L., Nanoflakes-Assembled Three-Dimensional Hollow-Porous V2O5 as Lithium Storage Cathodes with High-Rate Capacity. *Small* **2014**, *10* (15), 3032-3037.
36. Zhou, X.; Wu, G.; Gao, G.; Wang, J.; Yang, H.; Wu, J.; Shen, J.; Zhou, B.; Zhang, Z., Electrochemical Performance Improvement of Vanadium Oxide Nanotubes as Cathode Materials

for Lithium Ion Batteries through Ferric Ion Exchange Technique. *The Journal of Physical Chemistry C* **2012**, *116* (41), 21685-21692.

37. Sauvage, F.; Bodenez, V.; Tarascon, J.-M.; Poeppelmeier, K. R., Room-Temperature Synthesis Leading to Nanocrystalline Ag₂V₄O₁₁. *Journal of the American Chemical Society* **2010**, *132* (19), 6778-6782.

38. Patoux, S.; Richardson, T. J., Lithium insertion chemistry of some iron vanadates. *Electrochemistry Communications* **2007**, *9* (3), 485-491.

39. He, Q.; Gorlin, Y.; Patel, M. U.; Gasteiger, H. A.; Lu, Y.-C., Unraveling the correlation between solvent properties and sulfur redox behavior in lithium-sulfur batteries. *Journal of The Electrochemical Society* **2018**, *165* (16), A4027.

40. Lu, Y.-C.; He, Q.; Gasteiger, H. A., Probing the Lithium–Sulfur Redox Reactions: A Rotating-Ring Disk Electrode Study. *The Journal of Physical Chemistry C* **2014**, *118* (11), 5733-5741.

41. Nilsson, V.; Kotronia, A.; Lacey, M.; Edström, K.; Johansson, P., Highly Concentrated LiTFSI–EC Electrolytes for Lithium Metal Batteries. *ACS Applied Energy Materials* **2020**, *3* (1), 200-207.

42. Cao, R.; Chen, J.; Han, K. S.; Xu, W.; Mei, D.; Bhattacharya, P.; Engelhard, M. H.; Mueller, K. T.; Liu, J.; Zhang, J. G., Effect of the Anion Activity on the Stability of Li Metal Anodes in Lithium-Sulfur Batteries. *Advanced Functional Materials* **2016**, *26* (18), 3059-3066.

43. Park, C.; Kanduč, M.; Chudoba, R.; Ronneburg, A.; Risse, S.; Ballauff, M.; Dzubiella, J., Molecular simulations of electrolyte structure and dynamics in lithium–sulfur battery solvents. *Journal of Power Sources* **2018**, *373*, 70-78.

44. Rajput, N. N.; Murugesan, V.; Shin, Y.; Han, K. S.; Lau, K. C.; Chen, J.; Liu, J.; Curtiss, L. A.; Mueller, K. T.; Persson, K. A., Elucidating the solvation structure and dynamics of lithium polysulfides resulting from competitive salt and solvent interactions. *Chemistry of Materials* **2017**, *29* (8), 3375-3379.

45. Shi, F.; Pei, A.; Vailionis, A.; Xie, J.; Liu, B.; Zhao, J.; Gong, Y.; Cui, Y., Strong texturing of lithium metal in batteries. *Proceedings of the National Academy of Sciences* **2017**, *114* (46), 12138-12143.

46. Suo, L.; Hu, Y.-S.; Li, H.; Armand, M.; Chen, L., A new class of Solvent-in-Salt electrolyte for high-energy rechargeable metallic lithium batteries. *Nature Communications* **2013**, *4* (1), 1481.

47. Safari, M.; Kwok, C. Y.; Nazar, L. F., Transport Properties of Polysulfide Species in Lithium–Sulfur Battery Electrolytes: Coupling of Experiment and Theory. *ACS Central Science* **2016**, *2* (8), 560-568.

48. Duboué-Dijon, E.; Javanainen, M.; Delcroix, P.; Jungwirth, P.; Martinez-Seara, H., A practical guide to biologically relevant molecular simulations with charge scaling for electronic polarization. *The Journal of Chemical Physics* **2020**, *153* (5), 050901.

49. Kann, Z.; Skinner, J., A scaled-ionic-charge simulation model that reproduces enhanced and suppressed water diffusion in aqueous salt solutions. *The Journal of chemical physics* **2014**, *141* (10), 104507.

50. Leontyev, I.; Stuchebrukhov, A., Electronic continuum model for molecular dynamics simulations. *The Journal of chemical physics* **2009**, *130* (8), 02B609.

51. Leontyev, I.; Stuchebrukhov, A., Accounting for electronic polarization in non-polarizable force fields. *Physical Chemistry Chemical Physics* **2011**, *13* (7), 2613-2626.

52. Mason, P. E.; Wernersson, E.; Jungwirth, P., Accurate description of aqueous carbonate ions: an effective polarization model verified by neutron scattering. *The Journal of Physical Chemistry B* **2012**, *116* (28), 8145-8153.
53. Chen, J. S.; Diard, J. P.; Durand, R.; Montella, C., Hydrogen insertion reaction with restricted diffusion. Part 1. Potential step—EIS theory and review for the direct insertion mechanism. *Journal of Electroanalytical Chemistry* **1996**, *406* (1), 1-13.
54. Diard, J. P.; Le Gorrec, B.; Montella, C., Linear diffusion impedance. General expression and applications. *Journal of Electroanalytical Chemistry* **1999**, *471* (2), 126-131.